NASA/TM-20250004046

Turbulent Shock-Wave/Boundary-Layer Interactions Without Sidewall Effects at Mach 2.5, 3.0, and 3.5—PIV Measurements From 2024 Test Entry

Heath H. Reising
Glenn Research Center, Cleveland, Ohio

April 2025

NASA STI Program Report Series

Since its founding, NASA has been dedicated to the advancement of aeronautics and space science. The NASA scientific and technical information (STI) program plays a key part in helping NASA maintain this important role.

The NASA STI program operates under the auspices of the Agency Chief Information Officer. It collects, organizes, provides for archiving, and disseminates NASA's STI. The NASA STI program provides access to the NTRS Registered and its public interface, the NASA Technical Reports Server, thus providing one of the largest collections of aeronautical and space science STI in the world. Results are published in both non-NASA channels and by NASA in the NASA STI Report Series, which includes the following report types:

- TECHNICAL PUBLICATION.
  Reports of completed research or a major significant phase of research that present the results of NASA programs and include extensive data or theoretical analysis. Includes compilations of significant scientific and technical data and information deemed to be of continuing reference value. NASA counterpart of peer-reviewed formal professional papers but has less stringent limitations on manuscript length and extent of graphic presentations.

- TECHNICAL MEMORANDUM.
  Scientific and technical findings that are preliminary or of specialized interest, e.g., quick release reports, working papers, and bibliographies that contain minimal annotation. Does not contain extensive analysis.

- CONTRACTOR REPORT.
  Scientific and technical findings by NASA-sponsored contractors and grantees.

- CONFERENCE PUBLICATION.
  Collected papers from scientific and technical conferences, symposia, seminars, or other meetings sponsored or cosponsored by NASA.

- SPECIAL PUBLICATION.
  Scientific, technical, or historical information from NASA programs, projects, and missions, often concerned with subjects having substantial public interest.

- TECHNICAL TRANSLATION.
  English-language translations of foreign scientific and technical material pertinent to NASA's mission.

Specialized services also include organizing and publishing research results, distributing specialized research announcements and feeds, providing information desk and personal search support, and enabling data exchange services.

For more information about the NASA STI program, see the following:

- Access the NASA STI program home page at http://www.sti.nasa.gov

NASA/TM-20250004046

Turbulent Shock-Wave/Boundary-Layer Interactions Without Sidewall Effects at Mach 2.5, 3.0, and 3.5—PIV Measurements From 2024 Test Entry

Heath H. Reising
Glenn Research Center, Cleveland, Ohio

National Aeronautics and
Space Administration

Glenn Research Center
Cleveland, Ohio 44135

April 2025

This work was sponsored by the
Transformative Aeronautics Concepts Program.

Trade names and trademarks are used in this report for identification only. Their usage does not constitute an official endorsement, either expressed or implied, by the National Aeronautics and Space Administration.

Level of Review: This material has been technically reviewed by technical management.

This report is available in electronic form at https://www.sti.nasa.gov/ and https://ntrs.nasa.gov/

NASA STI Program/Mail Stop 050
NASA Langley Research Center
Hampton, VA 23681-2199

Turbulent Shock-Wave/Boundary-Layer Interactions Without Sidewall Effects at Mach 2.5, 3.0, and 3.5 — PIV Measurements From 2024 Test Entry

Heath H. Reising
National Aeronautics and Space Administration
Glenn Research Center
Cleveland, Ohio 44135

Abstract

The High-Mach Validation Experiments (HMVE) campaign was initiated as a follow-on to shock-wave/boundary-layer interaction (SWBLI) experiments previously completed in the NASA GRC 225 cm^2 Wind Tunnel at a freestream Mach number of 2.5. Data were collected at Mach 3.0 and 3.5 freestream conditions using the same set of 3 angles for the conical shock generators in the axisymmetric test section. Select cases from Mach 2.5 testing were also duplicated to verify repeatability. Particle image velocimetry (PIV) measurements were applied to collect large ensembles of velocity data which were stitched together to form a quasi-continuous view of the mean and turbulent flowfield behavior. Densely-spaced wall pressure measurements were concurrently acquired to supplement the flowfield information from PIV. The primary purpose of this report is to assess the quality of data obtained in this entry to guide subsequent test entries after which the comprehensive results will be analyzed in-depth. Herein, velocity data is visualized component-by-component in contour plot form to visually assess the ability of the PIV technique to capture detailed flow features and also used to quantify and correct for small displacements in the shock generator tip which occur due to the long cantilevered support. As the Mach number regime contained in the overall dataset is being expanded, results are presented in a fashion which highlights trends in the flowfield behavior with variation in that parameter.

Nomenclature

D = test section diameter, 17 cm
P = pressure
R_{TS} = test section radius ($D/2$)
Re_D = core flow Reynolds number based on test section hydraulic diameter
T = temperature
u = axial velocity (aligned with $\vec{x}$)
v = vertical velocity (aligned with $\vec{y}$)
w = spanwise velocity (aligned with $\vec{z}$)
x = axial coordinate, $x = 0$ at leading edge of test section
y = vertical coordinate, $y = 0$ on test section axis
$\overline{y}$ = wall-normal coordinate, $\overline{y} = 0$ at $(r, \theta) = (R, 180°)$
z = spanwise coordinate, $z = 0$ on test section axis
α = shock generator cone half-angle
θ = azimuth in cylindrical coordinate system, $\theta = 0$ at 12 o'clock and is clockwise positive looking upstream

Subscripts

i = inviscid shock impingement
t = total condition
w = wall

Special Notations

0 = facility nozzle exit station
1 = station at which incoming boundary layer is evaluated
∞ = freestream or boundary layer edge
$\overline{(\ )}$ = time average (Reynolds average)
$(\ )'$ = deviation of instantaneous value from the time average

I. Introduction

Validation of turbulence models is paramount in the pursuit of accurate computational fluid dynamics (CFD) predictions in the complex flowfields present in realistic aerospace vehicle and propulsion designs. Typically, methods which rely on modeling of the more complex fluid physics (e.g. Reynolds stresses and heat flux vector in Reynolds-averaged Navier-Stokes (RANS) simulations) are less expensive than scale-resolving methods such as Large-Eddy Simulation (LES) and can be used in parametric optimization studies. However, the models used within these lower-fidelity methods are almost universally calibrated in equilibrium turbulence and require careful tuning to accurately predict the production, transport, and dissipation of turbulence in complex flowfields. Shock-wave/boundary-layer interactions are typically identified as a problematic case for RANS solvers due to their large departure from an equilibrium turbulence state[1].

A dearth of high quality experimental data in supersonic and hypersonic shock-wave/boundary-layer interactions for use in code validation efforts was identified by Settles and Dodson [2]. There, many of the candidate datasets were rejected due to the lack of well-defined boundary conditions, undocumented 3D effects, inconsistency between repeated measurements, or a lack of repeated measurements. A specific methodology was laid out in Ref. 3 for planning useful CFD code validation experiments which acknowledges the interdependency between the requirements and capabilities of experimental and computational results.

In addition to the overall lack of high-quality experimental data, the influence of the glancing sidewall interaction is commingled with many nominally 2D SWBLI datasets. References 4 and 5 show just two examples where blockage generated by corner separations influence the strength of the primary SWBLI. Thus, the current campaign aims to use an axisymmetric wind tunnel test section and shock generator cone to circumvent this issue.

The High-Mach Validation Experiments (HMVE) are a follow-on to the Turbulent Computational Fluid Dynamics Validation Experiment (TCFDVE) campaign which was reported on in several papers [6–10]. These test entries comprise an ongoing effort funded by the Transformation Tools and Technologies project at NASA Glenn Research Center (GRC) to provide a high-quality experimental dataset of a SWBLI which is free of sidewall effects. A key component of a high-quality CFD validation dataset is the corroboration of a multitude of independent redundant measurements. This manuscript extends upon the previously reported results by exploring interactions at increased freestream Mach number.

II. Apparatus and Procedure

This report provides a complete summary of the PIV data collected in the test campaign completed in mid-June to early-July of 2024 as part of the High-Mach Validation Experiments (HMVE). PIV measurements were performed in the NASA Glenn Research Center 225 cm^2 Wind Tunnel. A schematic of the flowfield being studied is shown in Fig. 1. Simple cone-cylinder bodies were used to generate the initial shock wave which impinges on the naturally-occurring test section boundary layer. This provides a relatively thick profile in which to perform the detailed measurements required. The cone half-angle, α, was varied to provide both unseparated and separated interactions.

Figure 1 also gives a pictorial reference for the coordinate system and nomenclature used throughout this manuscript. Spatial coordinate are shown in both Cartesian (gray) and cylindrical (blue) systems to connect between the measurements and the axisymmetric geometry. While x is indicated to reference from the test section leading edge, the data is generally presented relative to the location of the inviscid shock impingement station. The directions for the defined velocity components which align with the typical convention for Cartesian coordinates are represented in green.

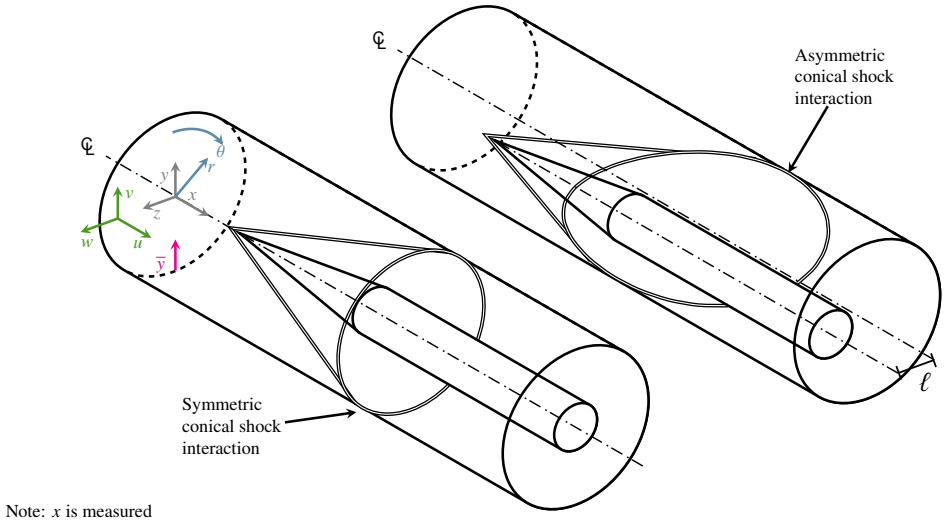

Fig. 1 Basic geometry and coordinate systems.

A. Test Facility

For the test results presented herein, the tunnel was configured with its axisymmetric 17 cm diameter test section and one of three converging-diverging nozzles: M2.5, M3.0, and M3.5. The wind tunnel and the specific test section geometry used for this test has been described thoroughly in Refs. 6–9.

The cone-cylinder centerbodies used to generate the impinging shock waves were highly configurable. Three tip cone half-angles were available to generate interactions of various strengths: 10° for an unseparated interaction, 13.5° for incipient separation, and 16° for a fully separated interaction. Typically, the cylindrical portion of the body was 5 cm in diameter and was comprised of a collection of spacer pieces to generate the desired axial length. A specific length of spacer stack was selected for each cone angle and Mach number to place the inviscid impingement at approximately the same axial station, with one key exception: for the current HMVE campaign, a larger version of the $\alpha = 16°$ cone was fabricated which continued the conical expansion out to a radius of 3 cm in an attempt to increase the compression length at the wall. This part contained the same length of cylindrical section as the smaller diameter version, resulting in the cone tip residing in a more forward position when using the same set of spacers. Thus, the inviscid impingement station for the $\alpha = 16°$ cases at M3.0 and M3.5 are shifted forward in the test section by 17.44 mm.

The cone-cylinders were cantilevered from a support strut spanning the aft end of the section. This strut had a sharp leading edge to reduce blockage and, thus, lower the minimum Reynolds number condition available for testing. Three mounting positions are available on the strut. A centerline position allows for the generation of an axisymmetric interaction while two offset positions generate swept interactions as shown in Fig. 1. The near-wall measurements were made at the $\theta = 180°$ position. Thus, a secondary vertical coordinate, $\overline{y} = y + R$, is defined (magenta in Fig. 1) which aligns the presented data with typical wall-referenced coordinates used when presenting boundary layer data.

The axisymmetric cases require sampling only in one x-r plane to fully describe the flowfield. The probe-based measurements took advantage of this feature to reduce the reach required for the probe mount and traversing apparatus. Likewise, this enabled the application of PIV measurement in this facility using a fixed laser sheet position and a local seeding technique. Due to the strong local flow angularity (see Ref. 9), the PIV technique was the only flowfield measurement applied in the swept interactions.

B. Measurement Techniques

The PIV system utilized herein is basically unchanged from previous data collection for a Mach 2.5 freestream condition [9]. The design process for the PIV system and the constraints for implementing the technique in this particular facility are described in Ref. 11.

C. Test Parameters

In this entry, PIV data was collected for all 3 conical shock generator tips installed on the tunnel axis to create axisymmetric interactions for each facility nozzle. Additionally, the shock generator was offset to the $\ell = R/4$ and $\theta = 270°$ position to study swept interaction for the new M3.0 and M3.5 configurations. For each test configuration, the facility total temperature was tightly controlled at (311.0 ± 0.3) K ((100.0 ± 0.5) °F) in order to create a nearly adiabatic condition at the test section walls. This serves two purposes: simplifying the boundary conditions applied in companion CFD calculations and also minimizing the collection of condensation on the exterior of the test section which can occlude the windows through which the PIV cameras view the flowfield. For each fixed-geometry nozzle, the total pressure of the supply air was controlled to maintain specific Reynolds number values at the exit station. These are referred to in terms of test section diameter as Re_D and the specific values at which tests were operated are summarized below in Table 1. The operating points are selected such that the blockage sustained in the diffuser by the probe traverse or PIV apparatus does not cause significant incursion of the shock train into the test section. At Mach 2.5, there is significant headroom between a minimum Reynolds number and the capability of the pressure air supply system and the two values in Table 1 were selected to match historical precedent rather than push these bounds (operation at $Re_D < 2 \times 10^6$ has been explored preliminarily). However, the latitude between these two limits wanes with increasing Mach number (vacuum pressure is unchanged) and, thus, values are selected to minimize the Reynolds number (with reasonable margin) to allow for better boundary layer resolution and reduced computational cost of companion CFD calculations.

Table 1 Freestream test conditions.

Nominal		Actual	
$M_{0,\infty}$	$Re_D \times 10^{-6}$	$M_{0,\infty}$	$Re_D \times 10^{-6}$
2.5	2	$2.49 \pm 0.01^{*}(\pm 1.8 \times 10^{-4})^{\dagger}$	2.01 ± 0.01 (± 0.016)
2.5	4	2.50 ± 0.01 ($\pm 8.8 \times 10^{-5}$)	4.02 ± 0.02 (± 0.016)
3	2.25	2.98 ± 0.01 ($\pm 2.7 \times 10^{-4}$)	2.26 ± 0.02 (± 0.026)
3.5	3	3.49 ± 0.01 ($\pm 3.4 \times 10^{-4}$)	3.02 ± 0.02 (± 0.042)

* Ranges indicate 2σ scatter in the values calculated by facility data system simultaneously with PIV data collection.
† Values in parentheses indicate the measurement uncertainty bounds based on instrument accuracy.

III. Results and Discussion

Analysis of the PIV data first requires a precise determination of the wall position within the PIV vector fields. This is obtained by close inspection of the near-wall mean axial velocity and turbulent shear behavior in the incoming boundary layer. Then, the inviscid shock location can be ascertained by tracing the region of peak negative divergence to correct for minor variations in the shock generator position, as described in the following section.

A. Axial Alignment of the Data from the PIV Configuration

As described in Ref. 9, the optical access required for PIV measurements necessitated the inclusion of a longer centerbody to provide enough axial clearance for the cameras to be placed between the region of interest and the flange at the aft end of the test section. Thus, while the test configurations are equivalent from the plenum tank to the interaction, the PIV configuration is more susceptible to misalignment of the cone-cylinder tip due to the longer cantilevered length. Great care was taken to ensure that the centerbody was aligned with the test section pre-test at atmospheric pressure and the methods used were validated in the TCFDVE campaign where very little shifting of the centerbody was observed. However, in the HMVE campaign, a small offset was observed in both the wall pressure and PIV data. This is illustrated first in the pressure profiles of Fig. 2 which were collected by swapping the instrumented window insert from $\theta = 0°$ (typical location during PIV testing) to the $\theta = 180°$ position where the offset in the peak pressure within the interaction is consistently shown to be ~2.0 mm at Mach 3.5 where the largest cantilevered length is required.

It is expected that this effect would be exacerbated at higher freestream Mach numbers since the centerbody tip must be shifted further forward to accommodate the flattening of the conical shock wave. This results in not only increased cantilevered length, but also higher sensitivity of the wall pressure profile to small displacements of the cone tip. If, for

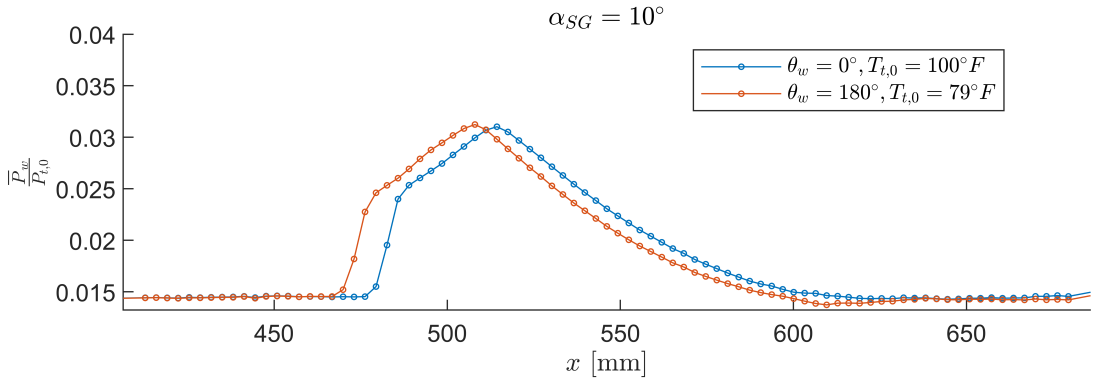

(a)

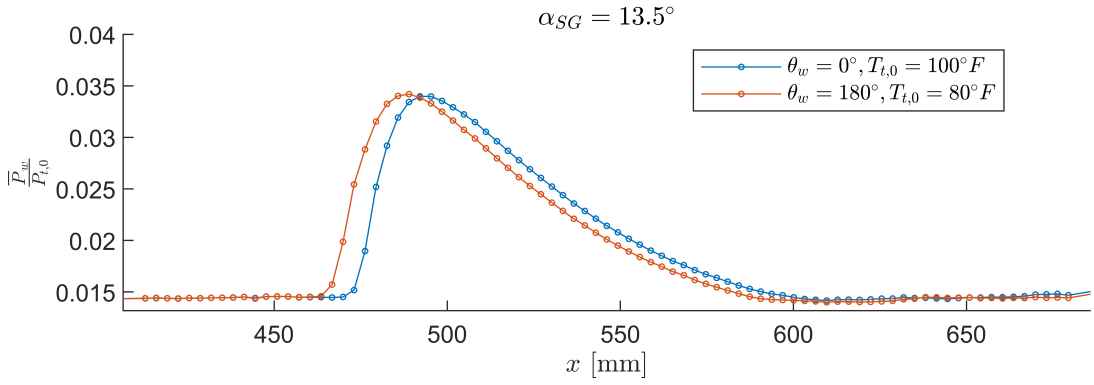

(b)

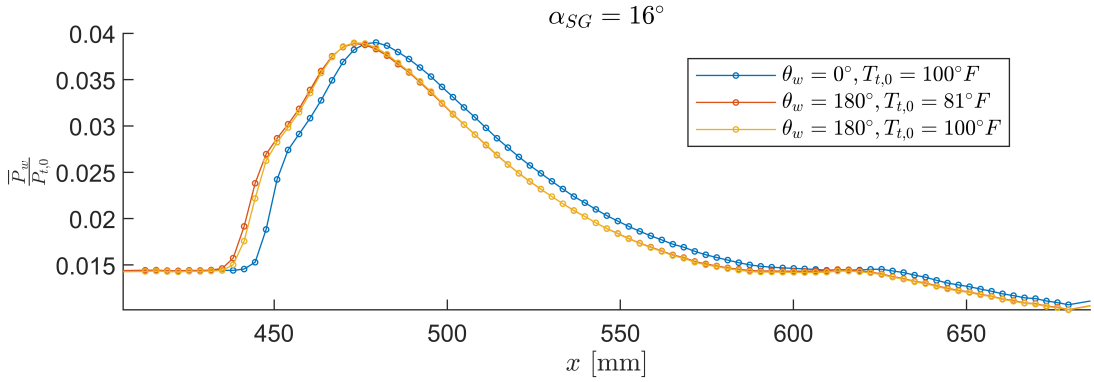

(c)

Fig. 2 Wall pressure profiles from instrumented window installed at $\theta = 0°$ and $\theta = 180°$ at M3.5.

example, the cone tip is assumed to be affected by a pure translation, then the resulting shift in the wall pressure profiles, Δx, as observed in Fig. 2 and the conical shock angle, β can be combined to predict the magnitude of the displacement, Δy, as

$$\Delta y = \frac{\Delta x}{2} \tan \beta \,. \tag{1}$$

This results in implied tip displacements of <1.5 mm, which is quite small when considering the 524 to 610 mm cantilevered length (shorter for low Mach number and larger α). For example, a rigid body rotation of the cone-cylinder about its mounting point of only 0.1 to 0.17° would cause the tip movement. A deflection this small would have a negligible effect on the shock strength, which aligns with the nearly identical character and peak value exhibited by the wall pressure profiles.

These measurements provide little information about the true inviscid impingement point since they only show the relative shift in the impingement between the top and bottom of the test section. Also, while the wall pressure profiles are collected with an instrumented window with densely-packed static taps, the spatial resolution of the profiles (3.2 mm = 1/8") is large relative to the shifts observed. Thus making a precise measurement of the centerbody offset based on these measurements is difficult.

By analyzing the velocity field produced by the PIV measurements, a second quantification of the offset can be made. Using the location of strongest negative divergence as the shock location surrogate proved to be the most reliable for fitting. This produced axial offset values of less than 1 mm for the axisymmetric cases from the TCFDVE campaign, which is in line with previous supposition of nearly zero offset during those installations. Applying this method to the data taken in axisymmetric configurations in the HMVE entry resulted in implied offsets of 3 to 6 mm at M2.5. Figure 3 illustrates the typical result by showing $\alpha = 16°$ case at M2.5.

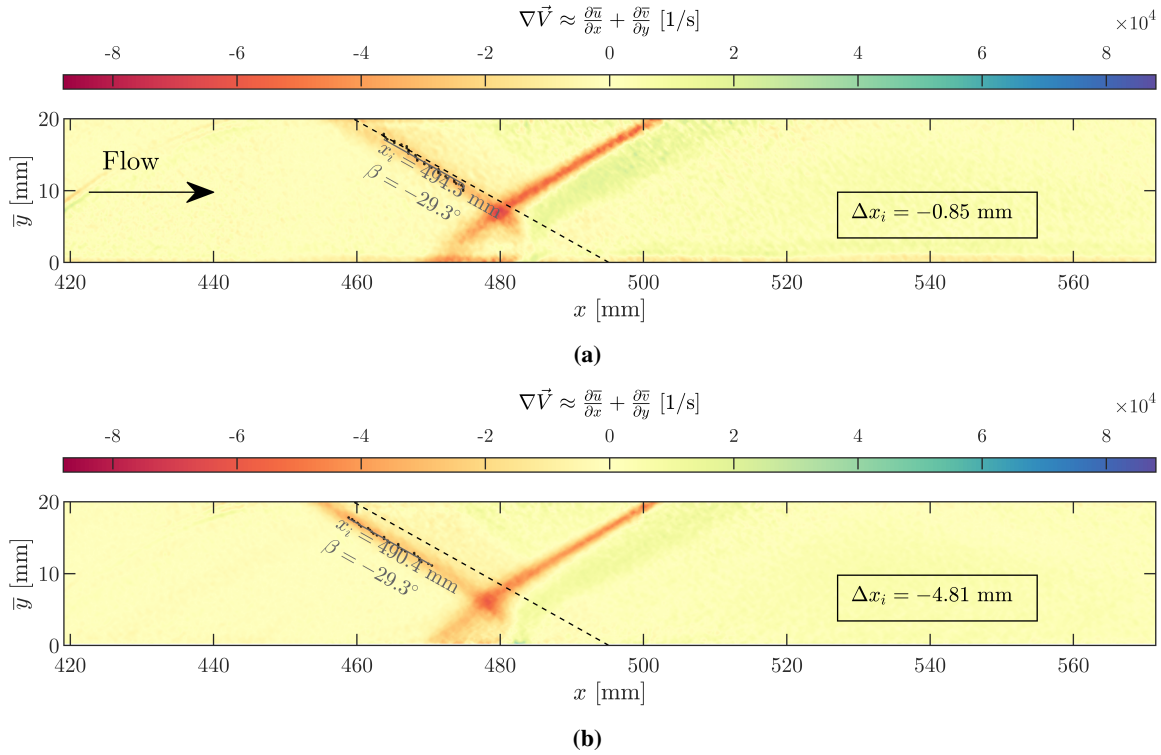

Fig. 3 Divergence fields showing best-fit impinging shock traces from (a) TCFDVE and (b) HMVE for axisymmetric configurations at M2.5, $\alpha = 16°$, and $Re_D = 4 \times 10^6$.

Similarly, the new cases at M3.0 and M3.5 were also analyzed using the same methods. Figure 4 presents the divergence fields from PIV measurements similar to Fig. 3 except that the color scale has been expanded to encompass the higher values that occur as Mach number increases. The shift in the inviscid impingement station observed for these cases is in line with what was observed at M2.5.

Table 2 summarizes the shifts observed over all the configurations sampled with PIV in this campaign. The outlier being the $\alpha = 10°$ is not unexpected since that configuration requires the largest cantilever for a particular Mach number. Additionally, the weak shock wave present in those cases makes precisely identifying the shock location more difficult, and the algorithmically-determined offset may be less accurate. For the swept configurations, the intersection of the inviscid conical shock with the measurement plane is no longer a straight line, but instead a conic section (hyperbola) which can be defined by

$$x = \frac{\sqrt{\ell^2 + (R - \bar{y})^2} - \sqrt{\ell^2 + R^2}}{\tan\beta} + x_i \,. \tag{2}$$

This equation was used to fit the shock front away from the boundary layer within the PIV data for the offset cases. Since the cone tip station was kept constant between the axisymmetric and swept configurations, there is an aftward

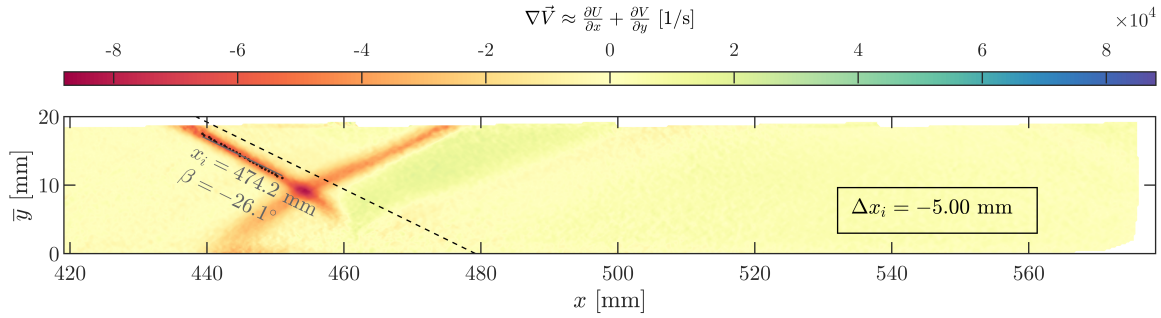

(a)

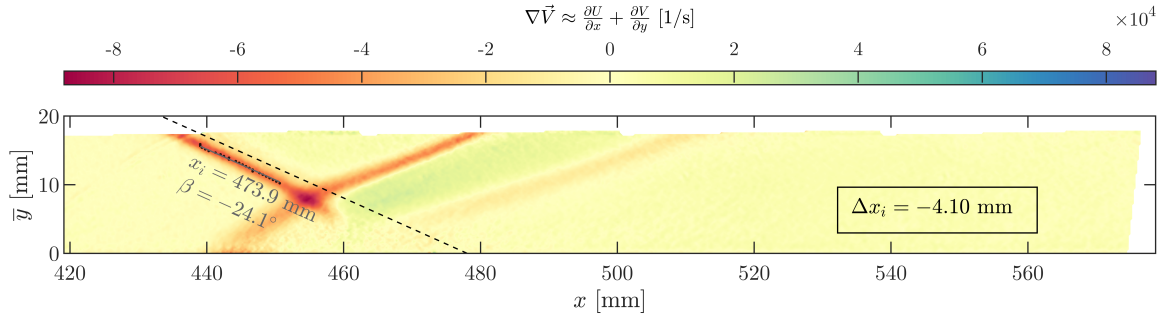

(b)

Fig. 4 Divergence fields showing best-fit impinging shock traces for axisymmetric configurations at (a) M3.0 and (b) M3.5 and $\alpha = 16°$.

shift in the nominal impingement station in the measurement plane of $R \cot\beta\sqrt{1 + \frac{\ell}{R}}$ which is typically on the order of 5 to 8 mm for the $\ell = R/4$ offset over the range of shock angles.

Table 2 Summary of measured inviscid impingement stations, x_i, inferred from PIV data.

		M2.5		M3.0	M3.5
		Re_D	Re_D	Re_D	Re_D
α	$\overline{\theta}$	2×10^6	4×10^6	2.25×10^6	3×10^6
10°	℄	488.5 (−5.9)	488.9 (−5.6)	488.3 (−6.4)	486.2 (−8.9)
	90°			499.1 (−2.2)	497.8 (−4.8)
13.5°	℄	490.9 (−5.2)	491.5 (−4.6)	490.1 (−4.1)	490.1 (−4.3)
	90°			497.8 (−2.2)	496.1 (−4.8)
16°	℄	491.8 (−3.4)	490.4 (−4.8)	474.2 (−5.0)	473.9 (−4.1)
	90°			482.9 (−1.7)	479.9 (−4.0)

Units are mm. Parenthetical is deviation from nominal location based on model geometry.

The existence of an offset for the M2.5 case, which did not use the new larger (heavier) $\alpha = 16°$ conical tip, implies that the use of a horizontal strut orientation also contributed somewhat to the droop since a vertical orientation was used for axisymmetric testing during the TCFDVE entry. However, no discernible droop was observed during probe surveys which necessitate a horizontal strut.

Because the location of the observed shock wave is also highly sensitive to the registration of the PIV images in the y-direction, a detailed analysis of the incoming boundary layer profiles to fit for the $\overline{y} = 0$ position will be pursued in

future analysis. However, the shifts derived from that analysis will be on the order of 0.1 mm and will not change the results in Table 2 drastically.

To make comparisons across the two test section configurations, data will be presented and compared in axial coordinates referenced to the inviscid impingement station determined for that particular configuration. In addition, run-to-run variation in the cone tip position will also be accounted for in the PIV results.

B. Wall Pressure Profiles

One way to confirm the shifts seen above is to check alignment of the wall pressure profiles from previous entries [9] with the current dataset using an axial coordinate normalized by the distance to the inferred shock position. Because the instrumented window is installed on the ceiling of the tunnel during PIV testing, the shift of the impinging shock location should be equal and opposite if due to a pure translation of the cone tip. Figure 5 shows the wall pressure profiles in corrected shock-referenced axial coordinates. It appears that the 16° case is very nearly a match to the previously collected data, indicating that the shift in cone tip position is not only accurately quantified, but also behaves like a pure vertical translation, as hypothesized. The other two profiles show discrepancies of 2 to 3 mm where the current profiles are shifted forward of their counterparts from the TCFDVE campaign. An analysis of previous data shows the shock impingement station to vary by ±2 mm between installations and, thus, the agreement seen here is within the typical precision of the hardware.

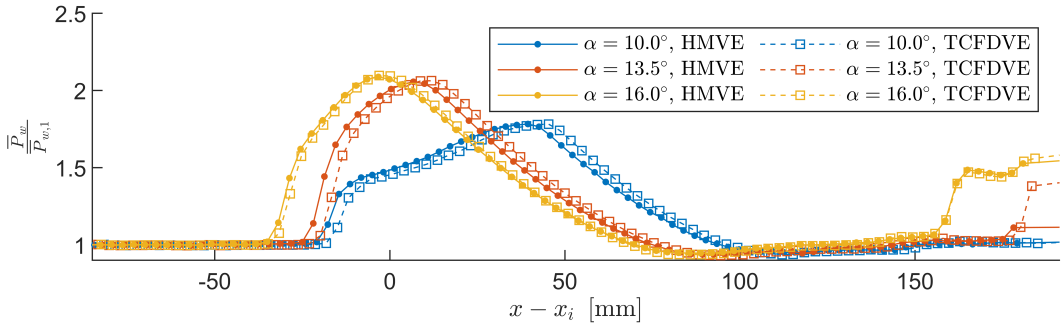

Fig. 5 Wall pressure profiles from instrumented window installed at $\theta = 0°$ in the axisymmetric configurations at M2.5 from current and previous test campaigns.

If we continue to assume the PIV-derived shock position is accurate, the wall pressure profiles corresponding to the new PIV flowfields at higher Mach numbers can then be inferred from measurements collected in the $\theta = 180°$ position. These are shown in Fig. 6. The primary difference in these profiles from the Mach 2.5 result is the increase in peak compression, which behaves as expected with increasing freestream Mach number. It is particularly evident in the $\alpha = 16°$ profiles since the increased length of the conical portion of the shock generator used in this entry separates the initial compression from the expansion emanating from the shoulder. This results in a larger upstream influence of the interaction.

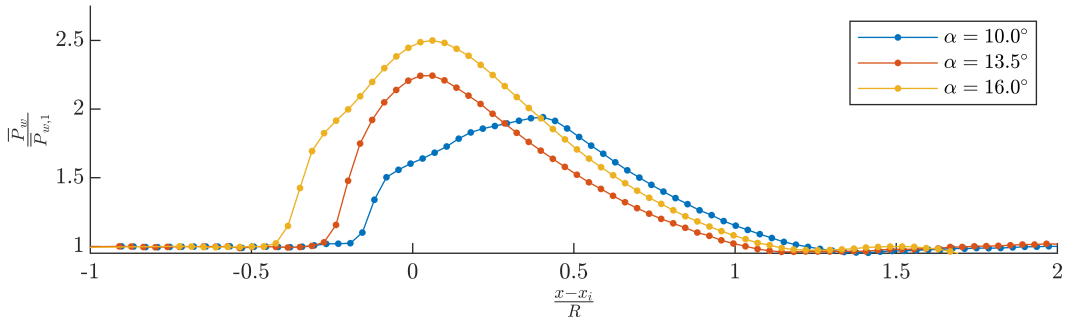

(a)

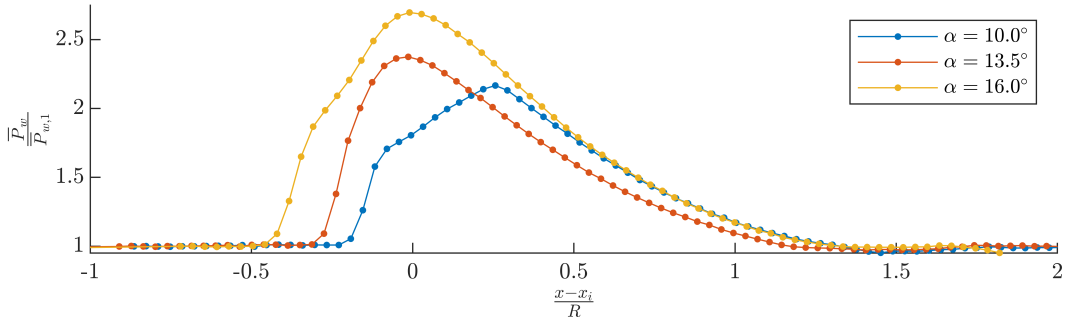

(b)

Fig. 6 Wall pressure profiles from instrumented window installed at $\theta = 180°$ in axisymmetric interactions at (a) M3.0 and (b) M3.5.

C. Qualitative Flowfield Comparisons

In this section, the stitched PIV fields from all camera views are presented for all three values of freestream Mach number across the various shock generator configurations to provide relative comparisons. For each, mean flow streamlines are overlaid to illustrate the overall flow behavior underlying the individual velocity components. For all subsequent figures, the lower Reynolds number operating point is presented as representative of the M2.5 cases such that Reynolds number is monotonically increasing with Mach number.

1. Unseparated Cases ($\alpha = 10°$)

Figures 7 and 8 show the mean velocity behavior for axisymmetric interactions emanating from shock waves generated by the shallowest conical centerbody. In the macroscopic sense, the behavior is similar with a slight increase in the extent of the defect in axial velocity with increasing freestream Mach number.

Figure 9 shows a direct comparison of the magnitude of turbulent fluctuations in axial velocity for the same axisymmetric interactions. These are again similar aside from the increase in scale of region of heightened turbulence downstream of the primary interaction. This is in line with the aforementioned increase in mean velocity disruption. Figure 10 shows the $u'v'$ shear turbulence intensity, which is again relatively unchanged with freestream Mach number in these weak interactions.

Figures 11 to 16 show comparisons of various flowfield quantities between the axisymmetric and swept cases for the high-Mach interactions in the near-interaction region at $\alpha = 10°$. In Fig. 11, the axial velocity deficit is shown to increase in magnitude and extend further upstream, regardless of freestream Mach number value. The region of upstream influence is seen to align closely with the region of significant through-plane velocity observed in Fig. 12, which reaches up to ~20% in these cases. Conversely, the intensity of turbulent fluctuations in the axial coordinate seems to vary strongly with Mach number between the two swept cases, with both showing higher magnitude than what is observed in their axisymmetric counterpart. For this value of α the through-plane turbulence is hardly changed, but the $u'w'$ turbulent shear does show a noticeable increase just upstream of the inviscid impingement location, especially at M3.5. The in-plane shear, however, is only minimally affected.

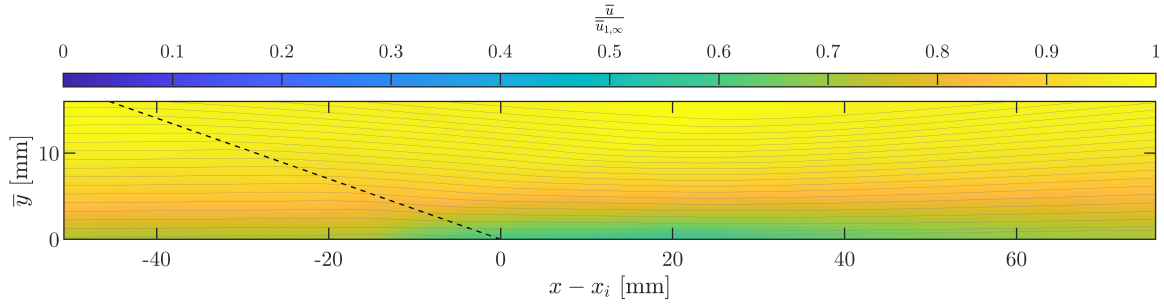

(a)

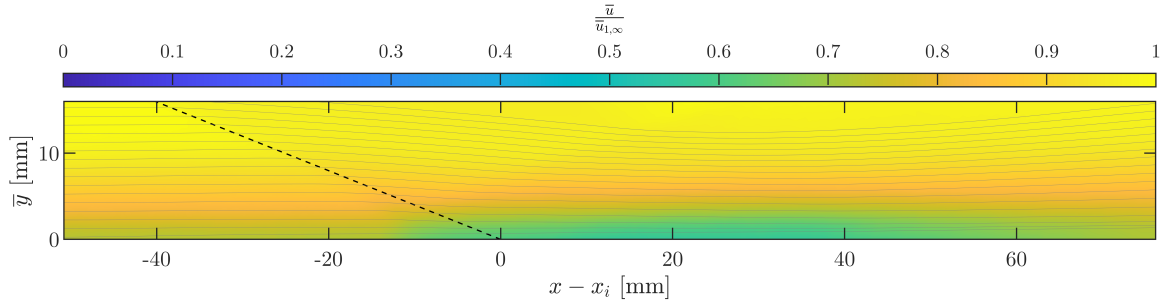

(b)

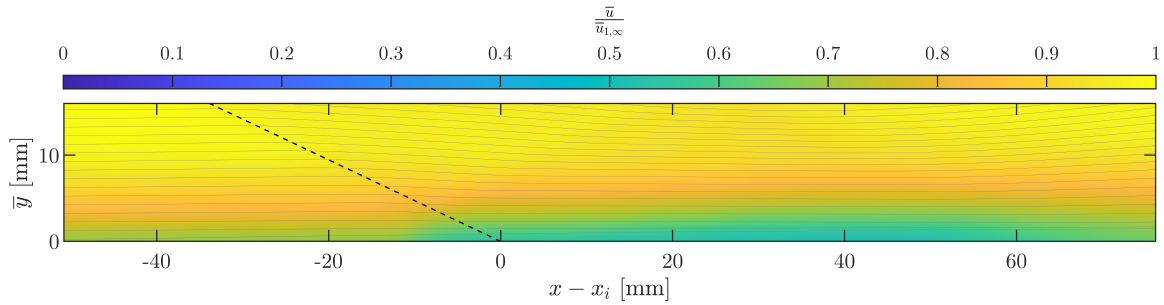

(c)

Fig. 7 Axial velocity fields in axisymmetric $\alpha = 10°$ interactions at (a) M3.5, (b) M3.0, and (c) M2.5.

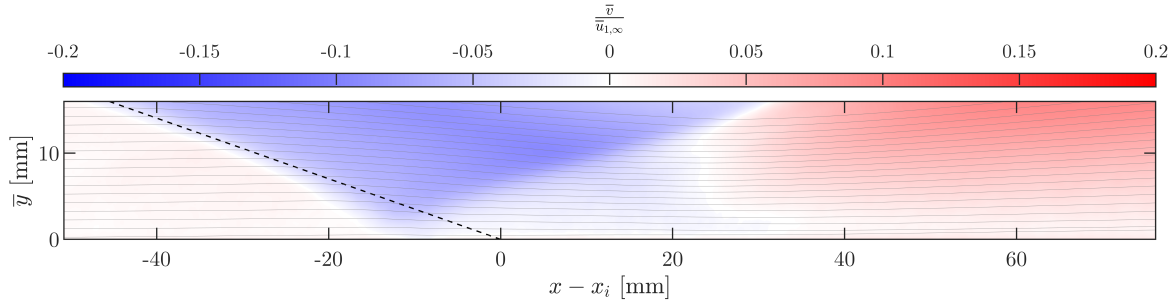

(a)

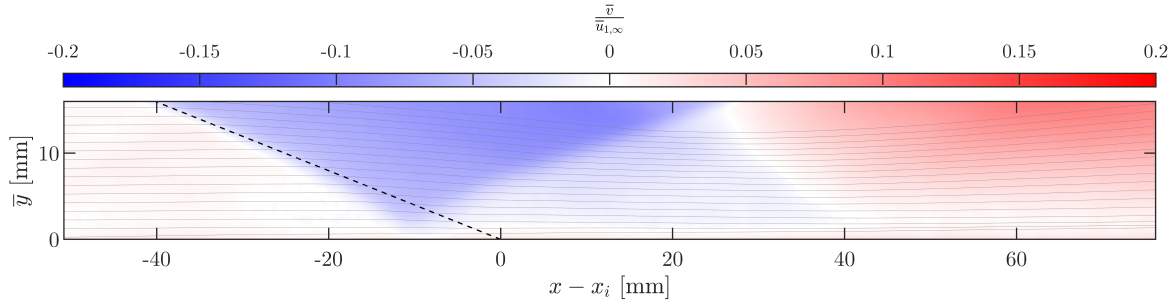

(b)

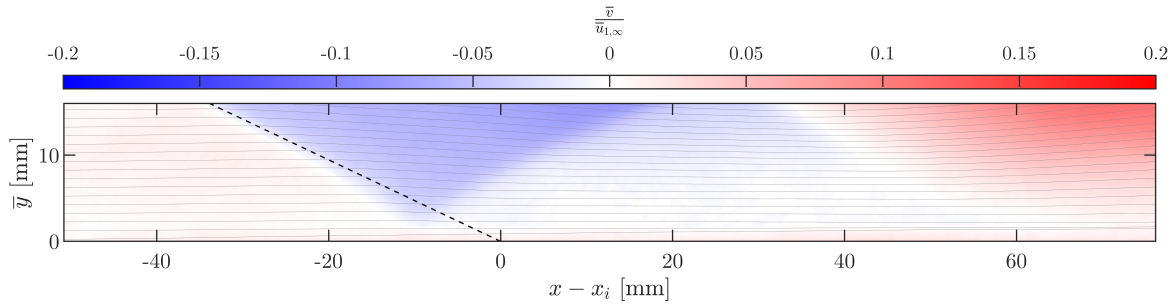

(c)

Fig. 8 Wall-normal velocity fields in axisymmetric $\alpha = 10°$ interactions at (a) M3.5, (b) M3.0, and (c) M2.5.

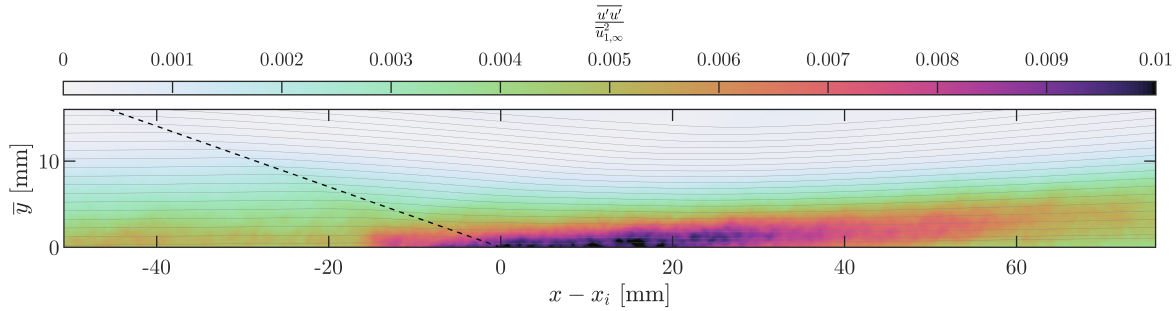

(a)

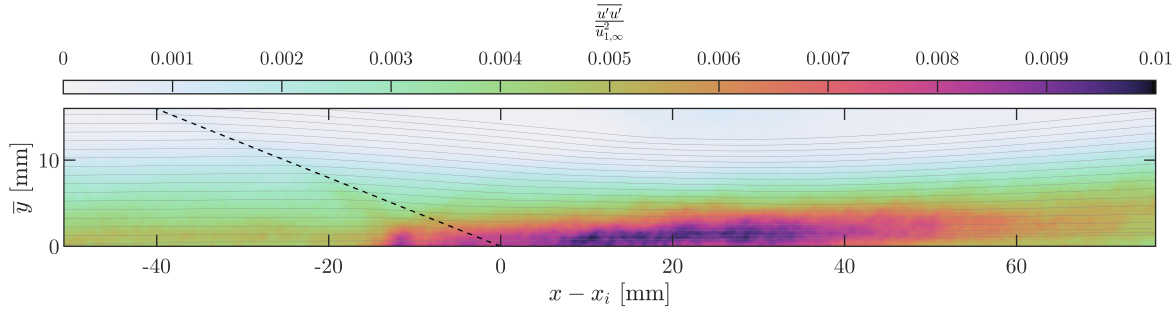

(b)

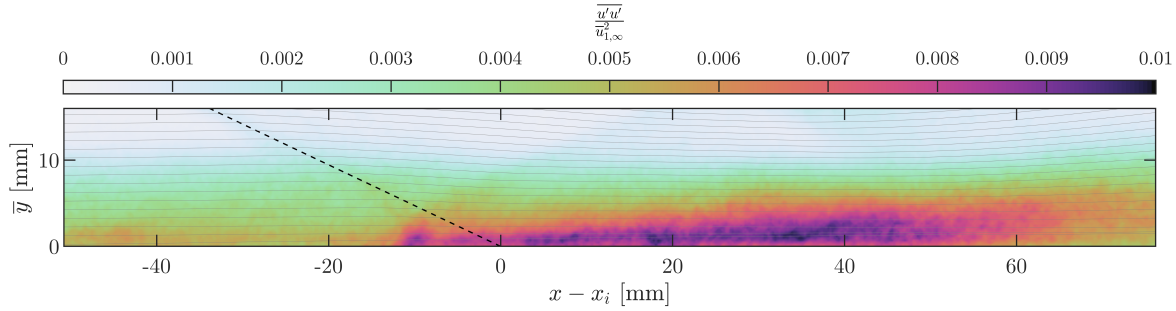

(c)

Fig. 9 Axial velocity turbulence intensity fields in axisymmetric $\alpha = 10°$ interactions at (a) M3.5, (b) M3.0, and (c) M2.5.

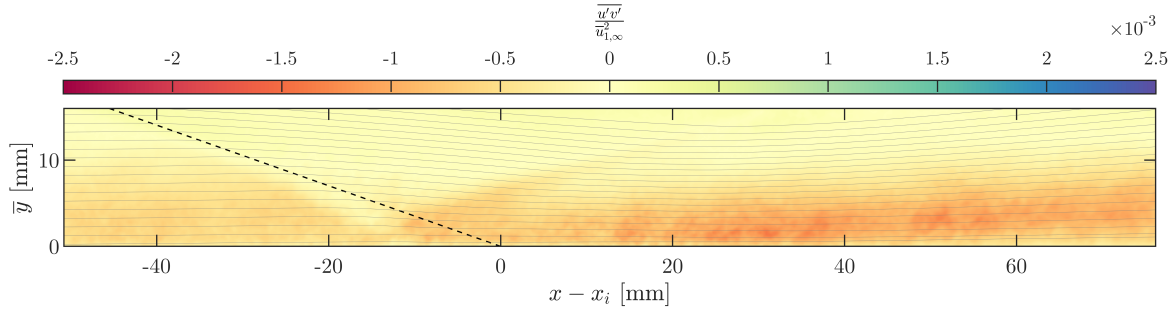

(a)

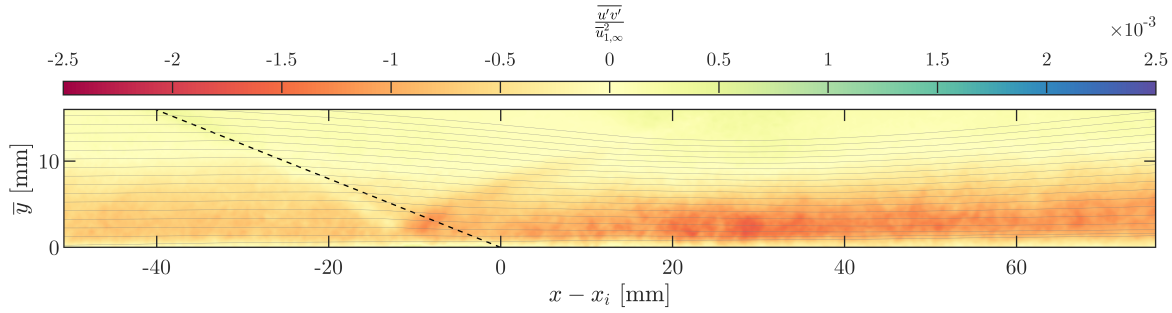

(b)

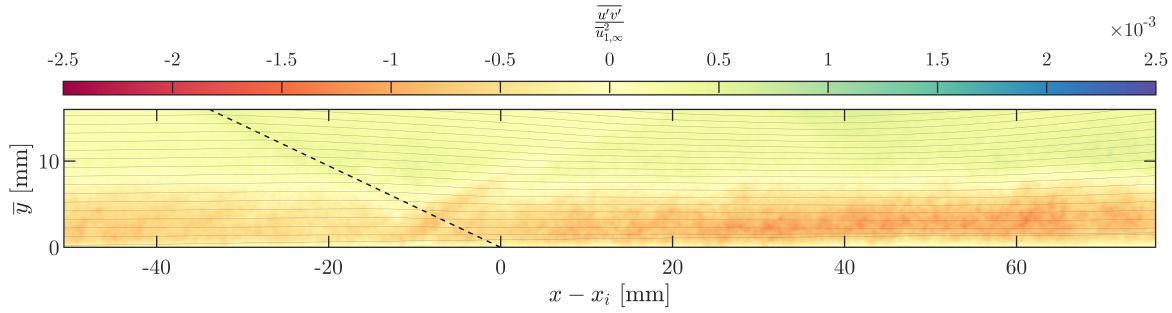

(c)

Fig. 10 Turbulent shear stress fields in axisymmetric $\alpha = 10^\circ$ interactions at (a) M3.5, (b) M3.0, and (c) M2.5.

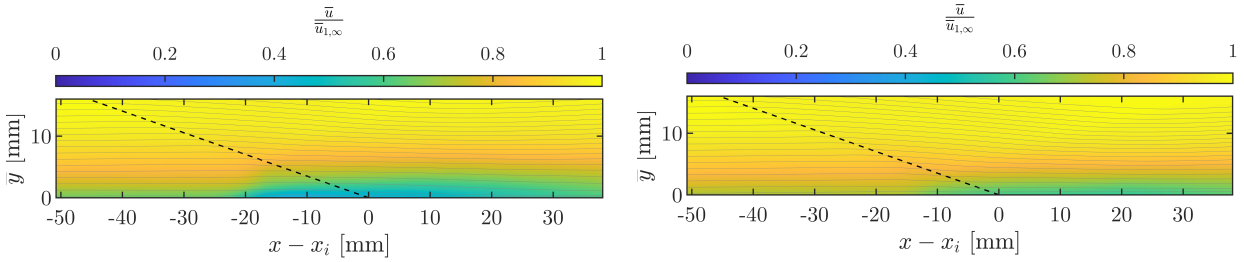

(a) M3.5, swept.

(b) M3.5, axisymmetric.

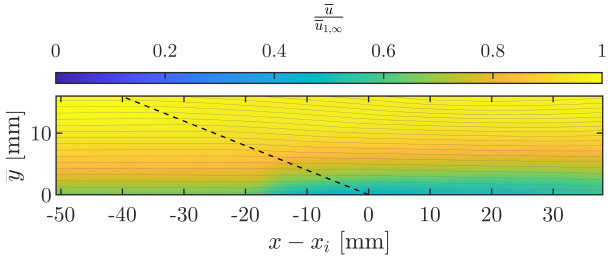

(c) M3.0, swept.

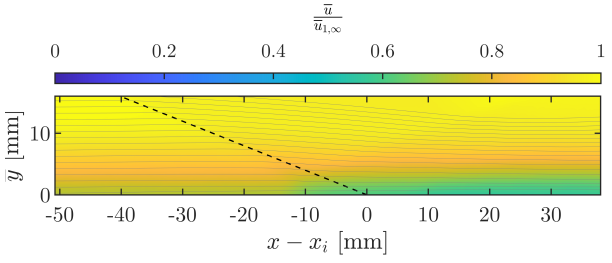

(d) M3.0, axisymmetric.

Fig. 11 Axial velocity field comparison between swept ($\ell = R_{TS}/4, \theta = 90°$) and axisymmetric ($\ell = 0$) interaction behavior near impingement at $\alpha = 10°$.

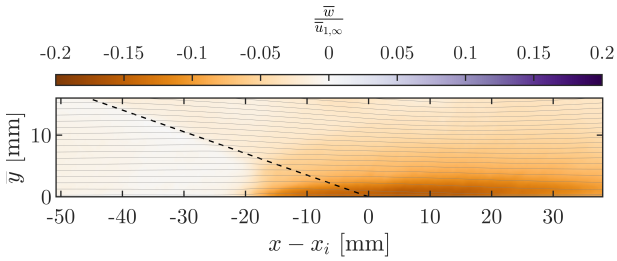

(a) M3.5, swept.

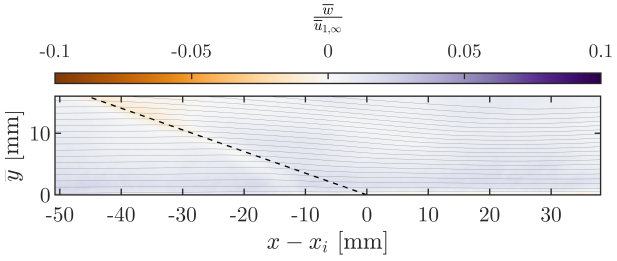

(b) M3.5, axisymmetric.

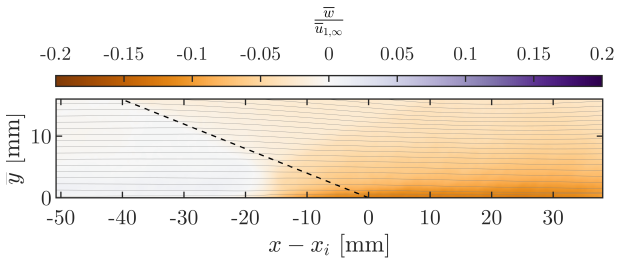

(c) M3.0, swept.

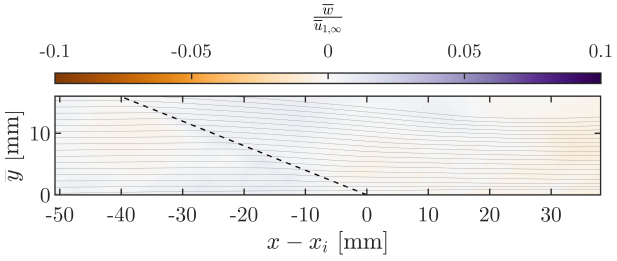

(d) M3.0, axisymmetric.

Fig. 12 Through-plane velocity field comparison between swept ($\ell = R_{TS}/4, \theta = 90°$) and axisymmetric ($\ell = 0$) interaction behavior near impingement at $\alpha = 10°$.

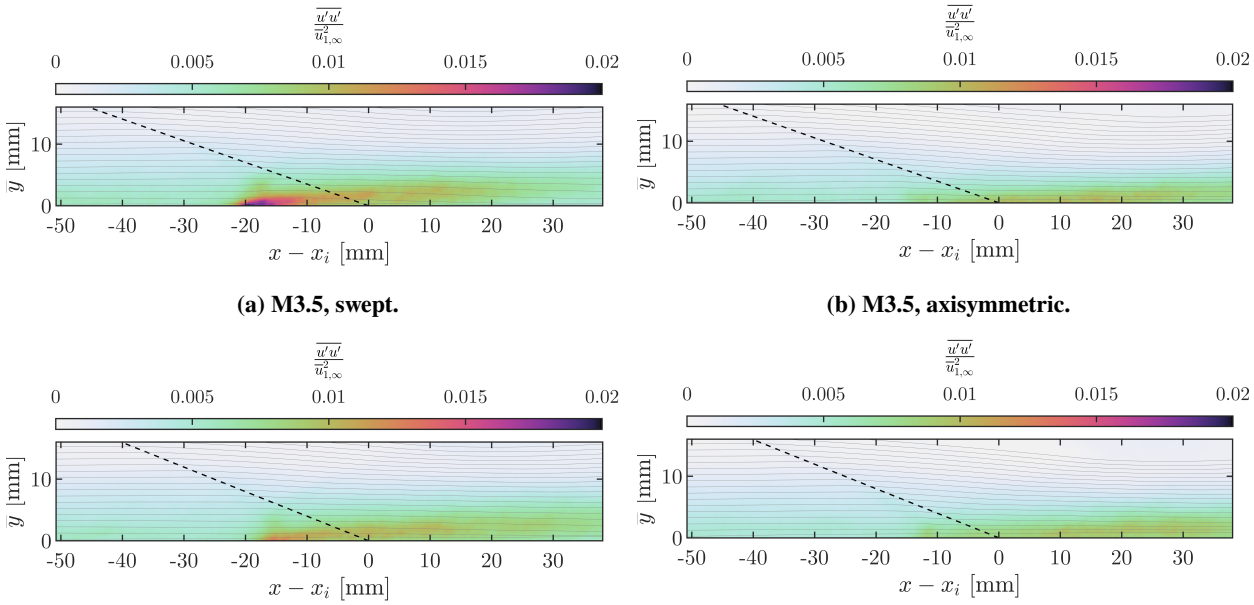

(a) M3.5, swept. **(b) M3.5, axisymmetric.**

(c) M3.0, swept. **(d) M3.0, axisymmetric.**

Fig. 13 Axial velocity turbulence intensity field comparison between swept ($\ell = R_{TS}/4, \theta = 90°$) and axisymmetric ($\ell = 0$) interaction behavior near impingement at $\alpha = 10°$.

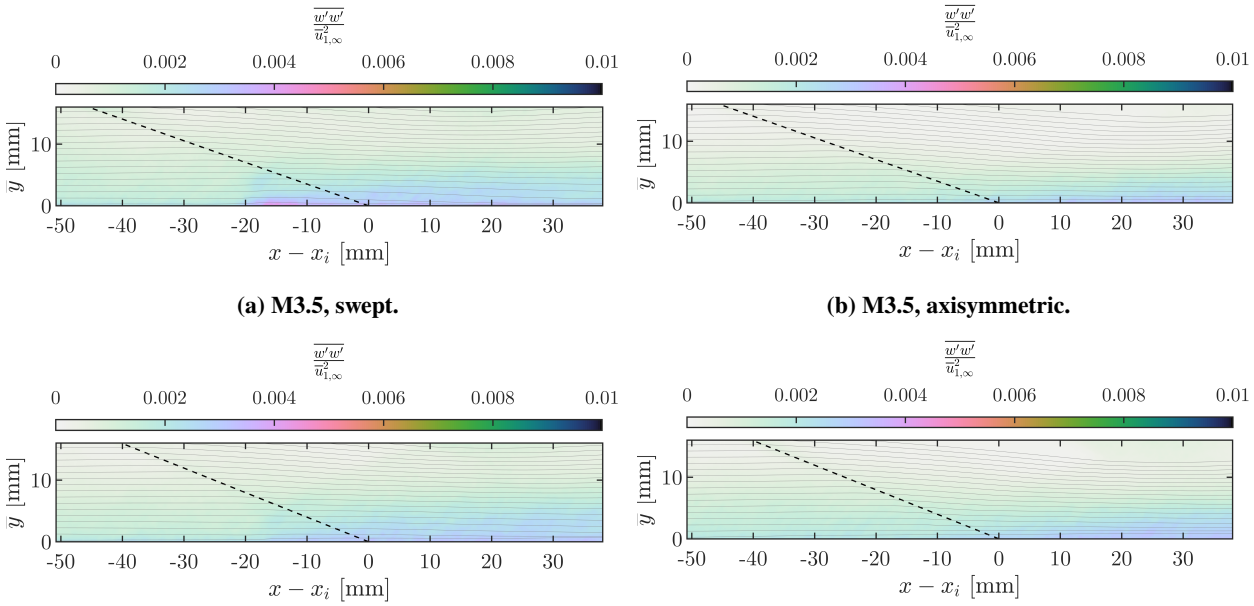

(a) M3.5, swept. **(b) M3.5, axisymmetric.**

(c) M3.0, swept. **(d) M3.0, axisymmetric.**

Fig. 14 Through-plane velocity turbulence intensity field comparison between swept ($\ell = R_{TS}/4, \theta = 90°$) and axisymmetric ($\ell = 0$) interaction behavior near impingement at $\alpha = 10°$.

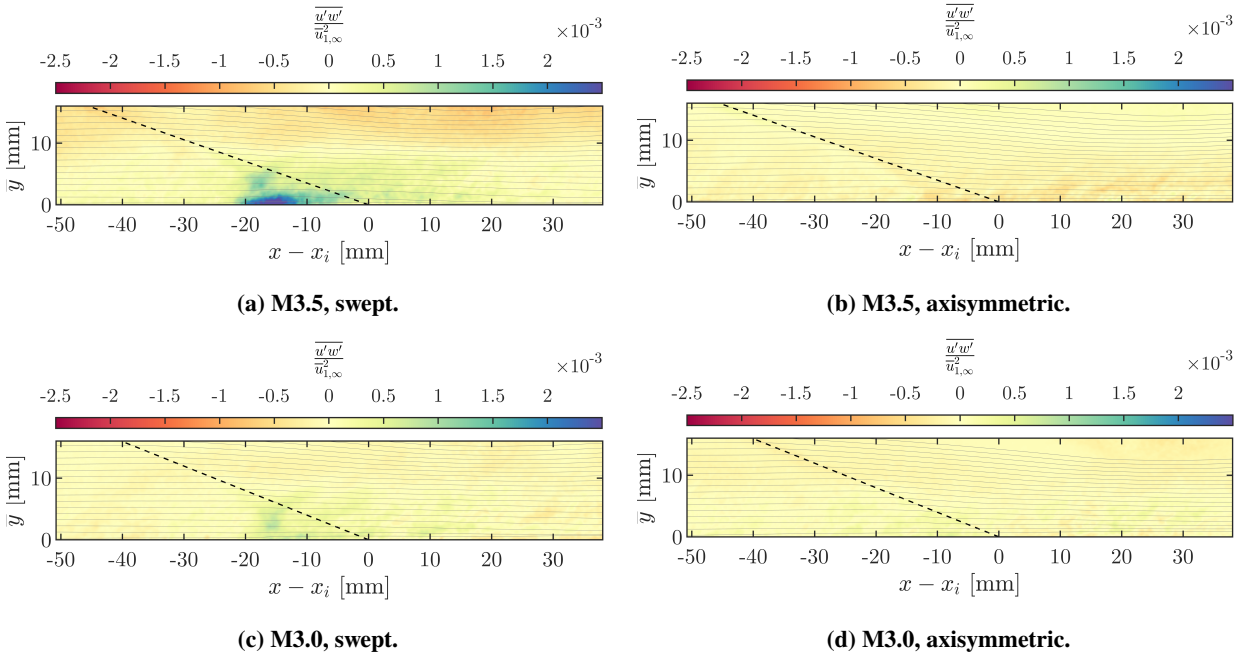

(a) M3.5, swept. **(b) M3.5, axisymmetric.**

(c) M3.0, swept. **(d) M3.0, axisymmetric.**

Fig. 15 x-z **plane turbulent shear stress field comparison between swept** ($\ell = R_{TS}/4, \theta = 90°$) **and axisymmetric** ($\ell = 0$) **interaction behavior near impingement at** $\alpha = 10°$**.**

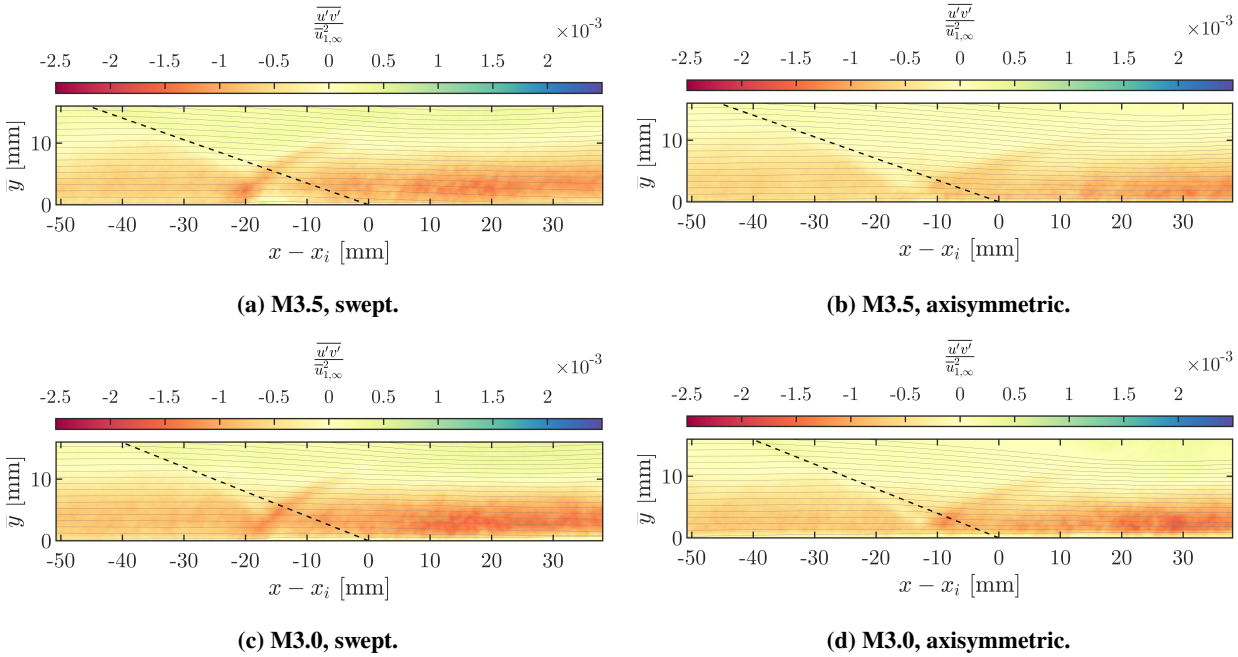

(a) M3.5, swept. **(b) M3.5, axisymmetric.**

(c) M3.0, swept. **(d) M3.0, axisymmetric.**

Fig. 16 In-plane turbulent shear stress field comparison between swept ($\ell = R_{TS}/4, \theta = 90°$) **and axisymmetric** ($\ell = 0$) **interaction behavior near impingement at** $\alpha = 10°$**.**

2. Incipient Separation Cases (α = 13.5°)

Figures 17 and 18 show the mean velocity behavior for axisymmetric interactions emanating from shock waves generated by conical centerbody of intermediate angle. Here, the dependence on freestream Mach number becomes more pronounced. This is likely due primarily to the increased pressure rise generated by the increasingly stronger shock waves for a fixed cone angle. Similarly, in Fig. 19, the axial component of turbulence is seen to be increasing rapidly with freestream Mach number with a tightly-concentrated peak region near the location of furthest upstream influence observed in the mean field. This likely coincides with higher occurrence of separation as the impinging shock strength rises. The in-plane shear turbulence shown in Fig. 20, on the other hand, appears to be much less sensitive to freestream Mach number.

Figures 21 to 26 show comparisons of various flowfield quantities between the axisymmetric and swept cases for the high-Mach interactions in the near-interaction region at α = 13.5°. As with the α = 10° cases, the swept interactions show a larger upstream incursion of the region of axial velocity defect. Here, the through-plane velocity has risen slightly on a normalized basis, is more concentrated to the interaction region, and is somewhat higher in magnitude for the M3.5 case over M3.0. At this value of α, the axial turbulence intensities are significantly reduced from the axisymmetric counterparts, as previously observed in the M2.5 campaign [9], while the through-plane component is now somewhat elevated and distributed further forward of the impingement point. Figure 25 illustrates the rise in $u'w'$ shear which significantly exceeds the intensity observed at lower α. The in-plane shear, on the other hand, is relatively insensitive to sweep.

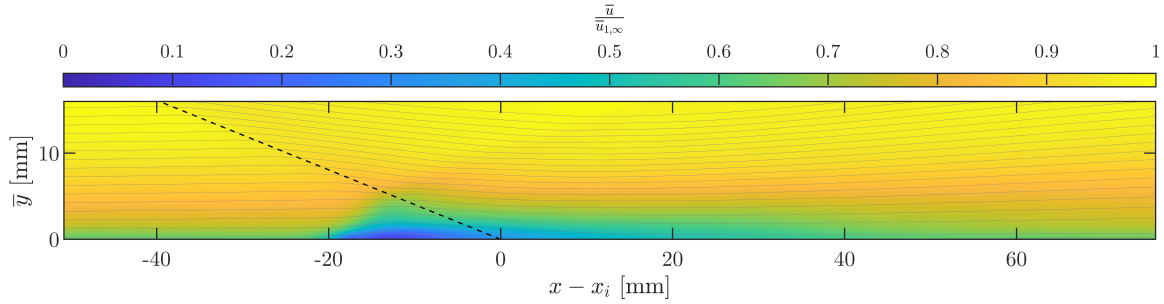

(a)

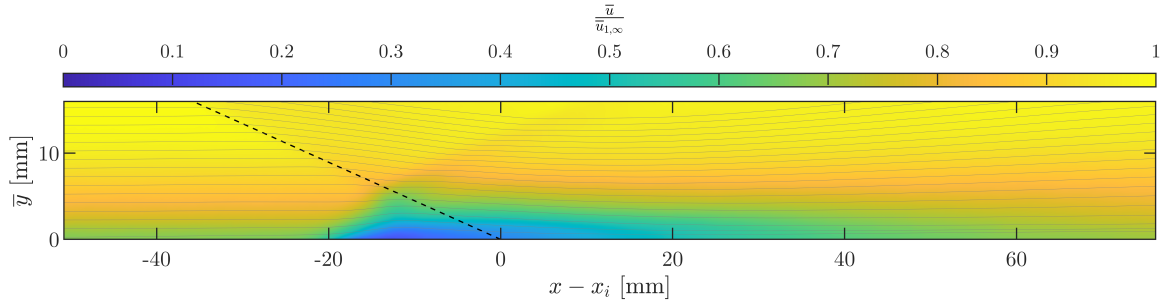

(b)

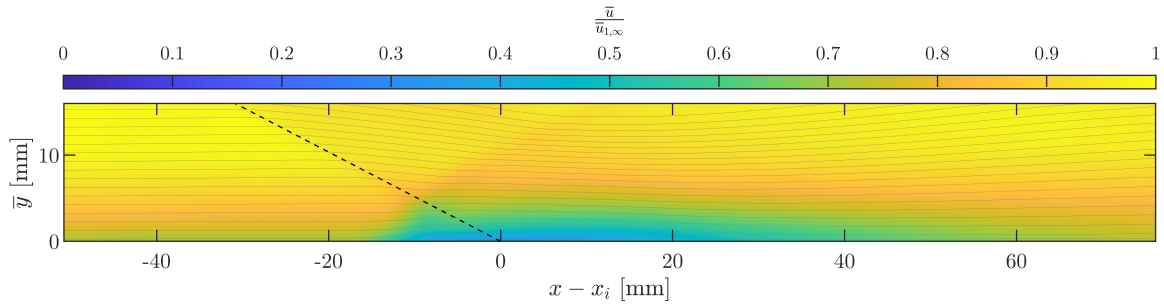

(c)

Fig. 17 Axial velocity fields in axisymmetric $\alpha = 13.5°$ interactions at (a) M3.5, (b) M3.0, and (c) M2.5.

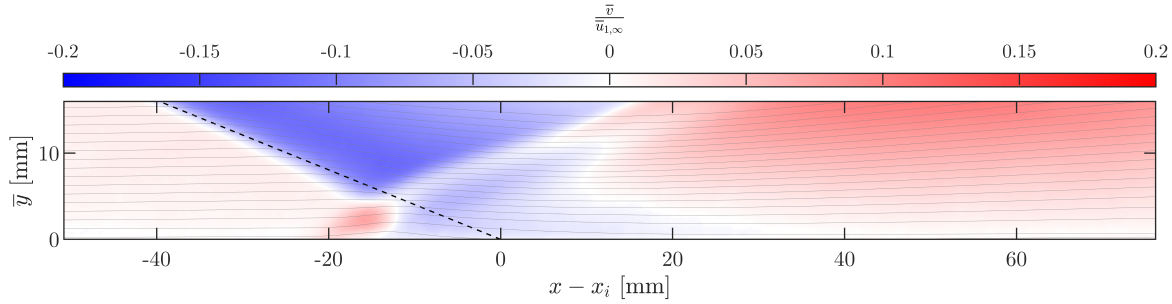

(a)

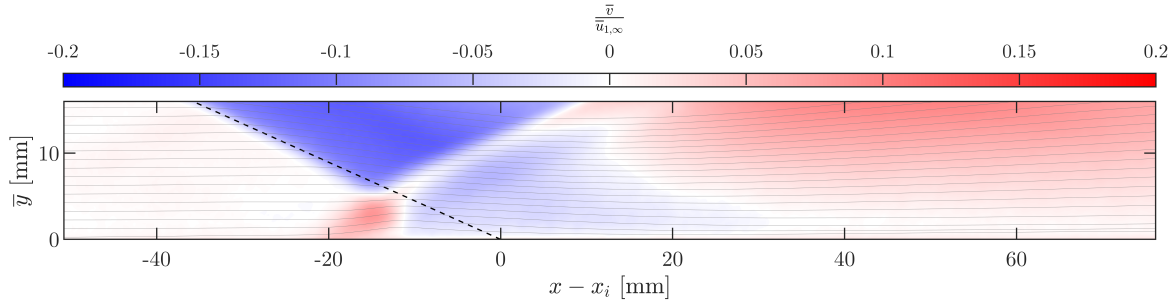

(b)

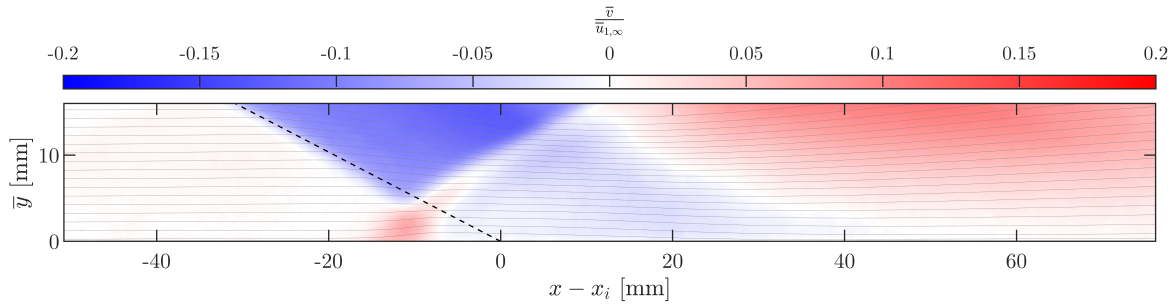

(c)

Fig. 18 Wall-normal velocity fields in axisymmetric $\alpha = 13.5°$ interactions at (a) M3.5, (b) M3.0, and (c) M2.5.

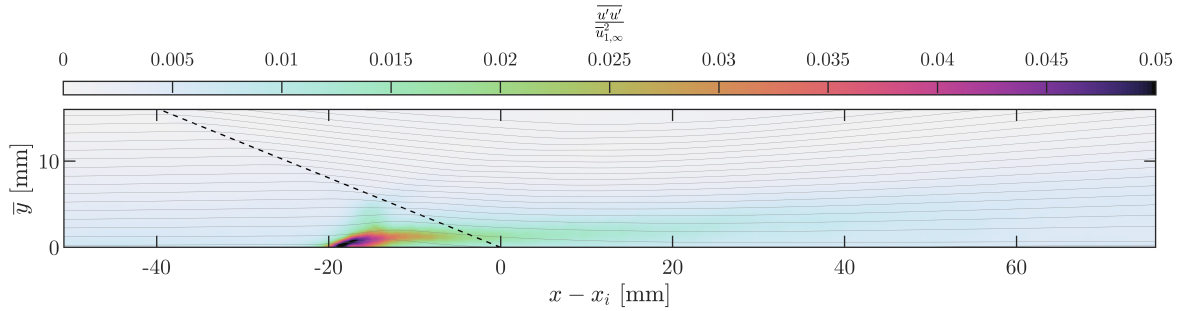

(a)

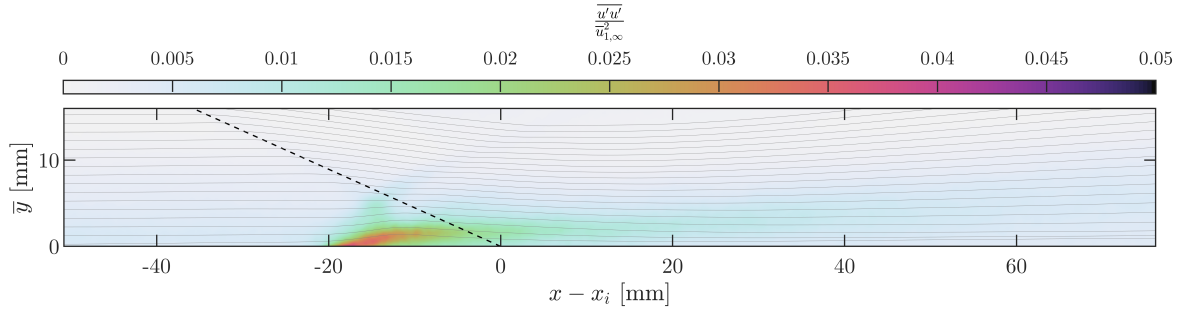

(b)

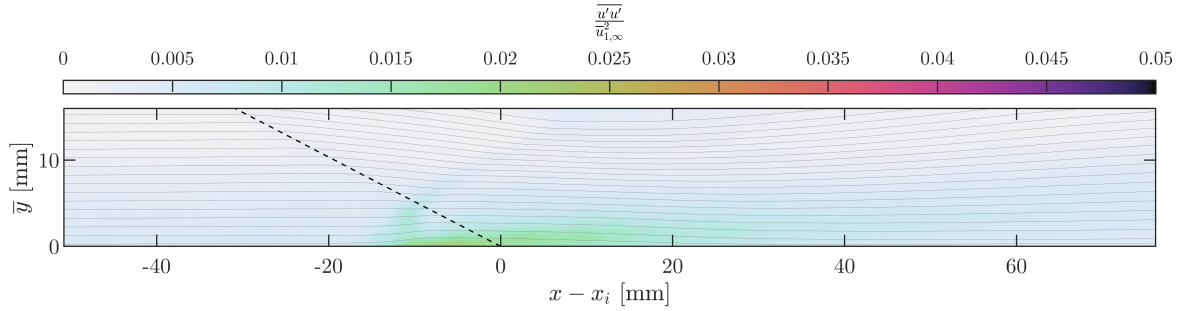

(c)

Fig. 19 Axial velocity turbulence intensity fields in axisymmetric $\alpha = 13.5°$ interactions at (a) M3.5, (b) M3.0, and (c) M2.5.

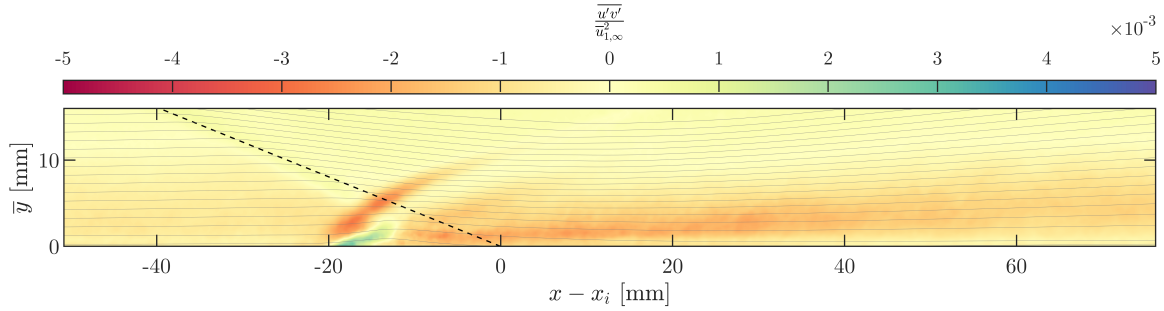

(a)

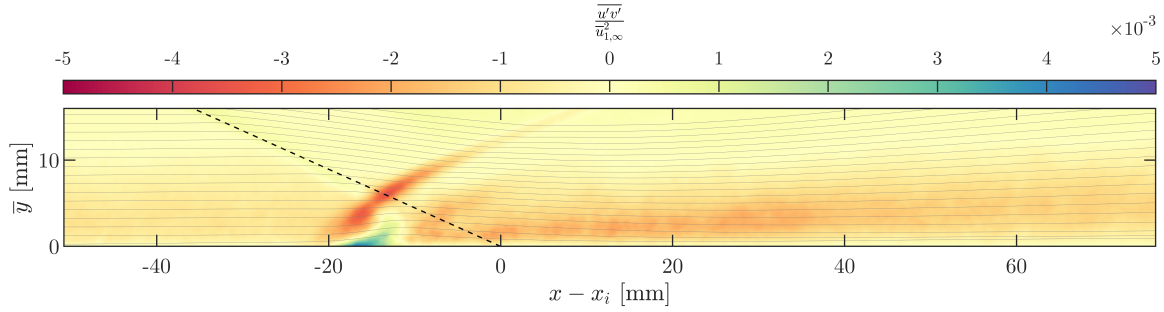

(b)

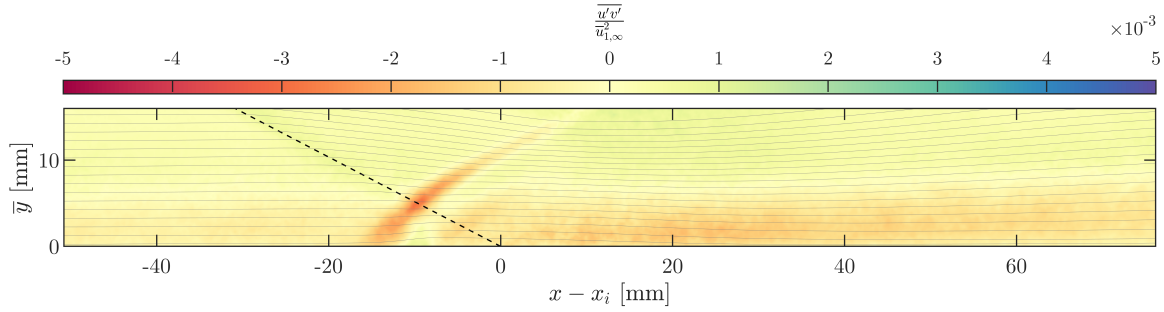

(c)

Fig. 20 Turbulent shear stress fields in axisymmetric $\alpha = 13.5°$ interactions at (a) M3.5, (b) M3.0, and (c) M2.5.

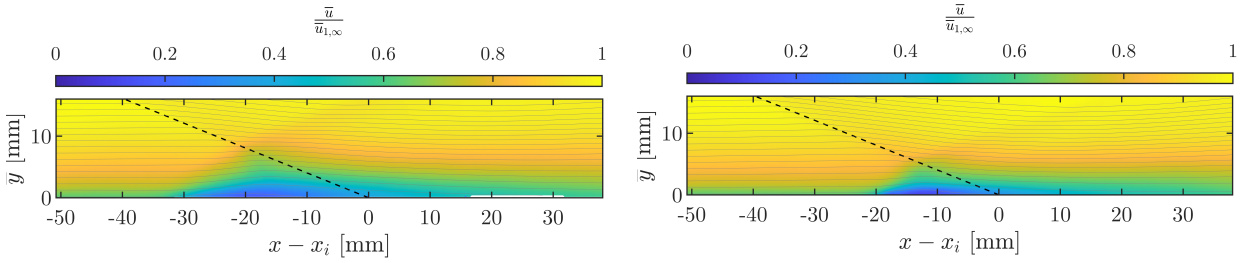

(a) M3.5, swept.

(b) M3.5, axisymmetric.

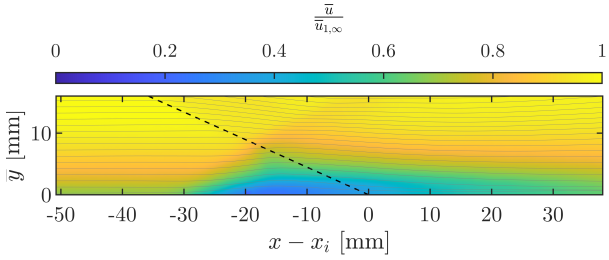

(c) M3.0, swept.

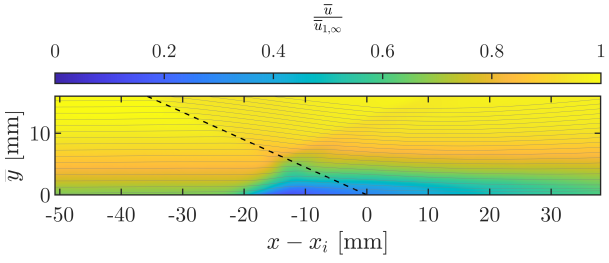

(d) M3.0, axisymmetric.

Fig. 21 Axial velocity field comparison between swept ($\ell = R_{TS}/4, \theta = 90°$) and axisymmetric ($\ell = 0$) interaction behavior near impingement at $\alpha = 13.5°$.

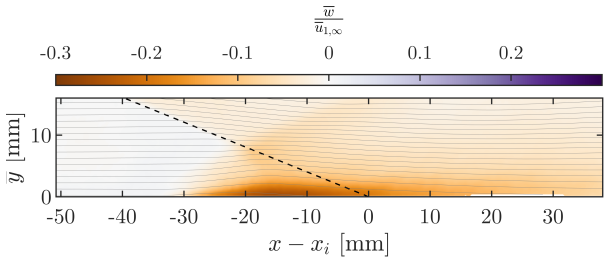

(a) M3.5, swept.

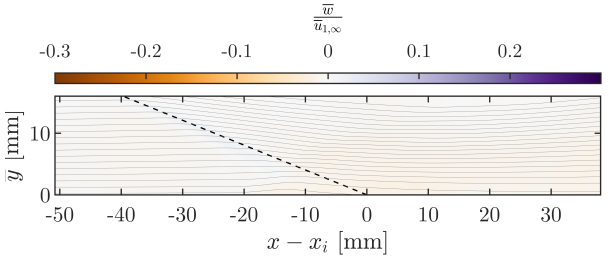

(b) M3.5, axisymmetric.

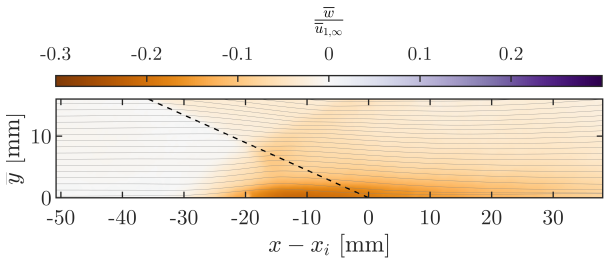

(c) M3.0, swept.

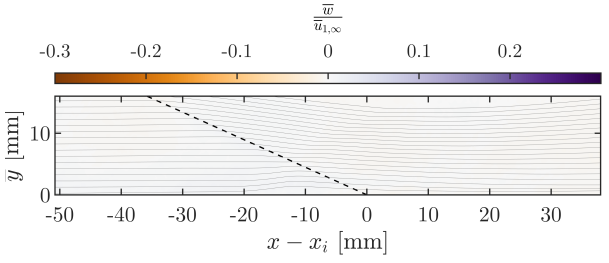

(d) M3.0, axisymmetric.

Fig. 22 Through-plane velocity field comparison between swept ($\ell = R_{TS}/4, \theta = 90°$) and axisymmetric ($\ell = 0$) interaction behavior near impingement at $\alpha = 13.5°$.

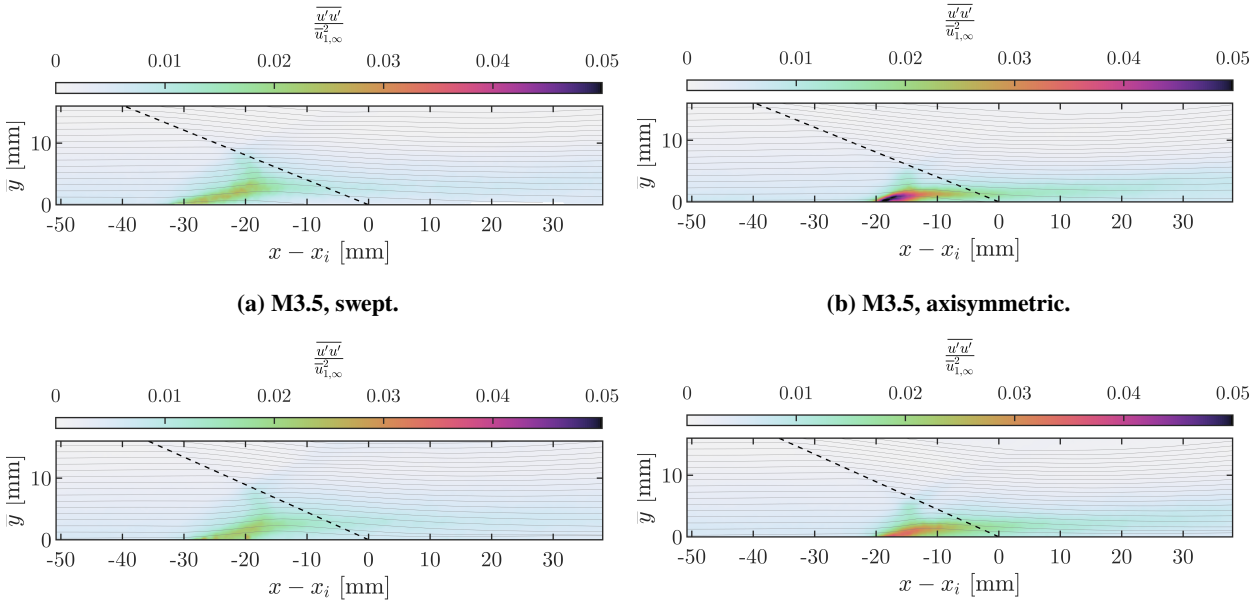

(a) M3.5, swept. **(b) M3.5, axisymmetric.**

(c) M3.0, swept. **(d) M3.0, axisymmetric.**

Fig. 23 Axial velocity turbulence intensity field comparison between swept ($\ell = R_{TS}/4, \theta = 90°$) and axisymmetric ($\ell = 0$) interaction behavior near impingement at $\alpha = 13.5°$.

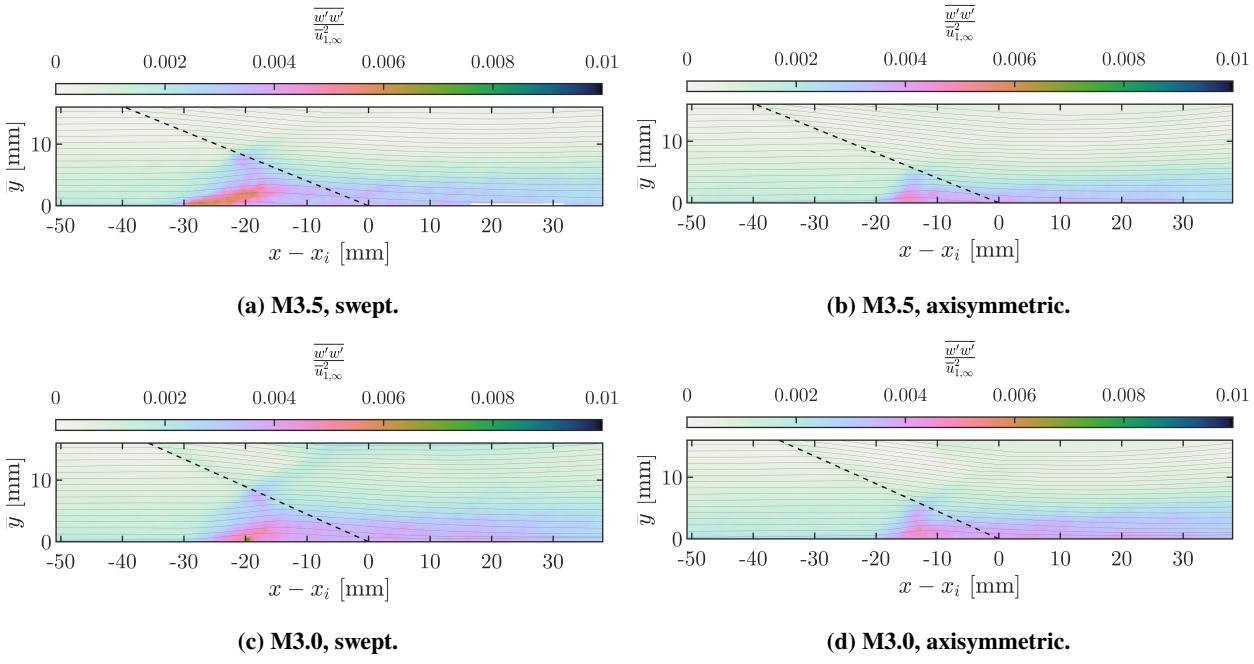

(a) M3.5, swept. **(b) M3.5, axisymmetric.**

(c) M3.0, swept. **(d) M3.0, axisymmetric.**

Fig. 24 Through-plane velocity turbulence intensity field comparison between swept ($\ell = R_{TS}/4, \theta = 90°$) and axisymmetric ($\ell = 0$) interaction behavior near impingement at $\alpha = 13.5°$.

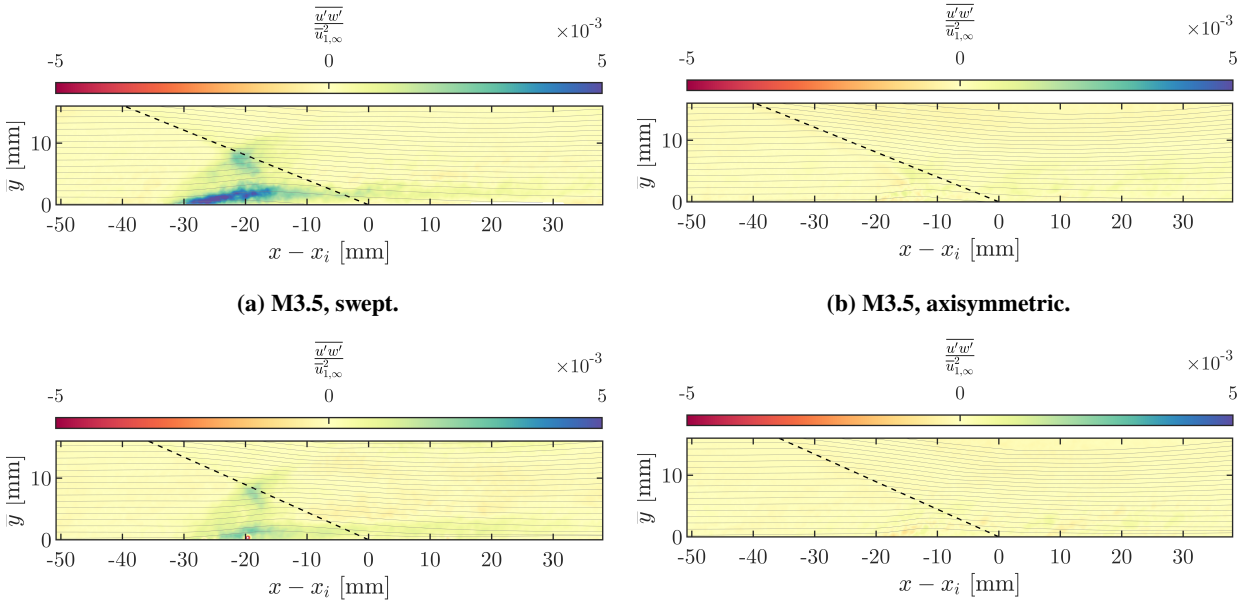

(a) M3.5, swept. **(b) M3.5, axisymmetric.**

(c) M3.0, swept. **(d) M3.0, axisymmetric.**

Fig. 25 x-z **plane turbulent shear stress field comparison between swept** ($\ell = R_{TS}/4, \theta = 90°$) **and axisymmetric** ($\ell = 0$) **interaction behavior near impingement at** $\alpha = 13.5°$**.**

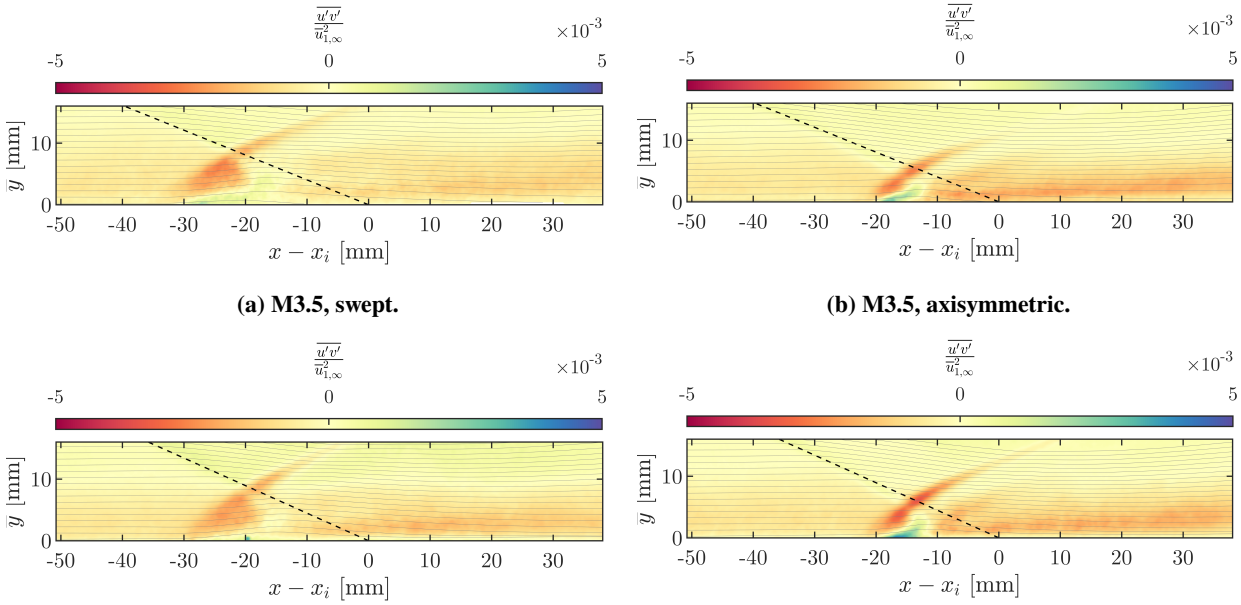

(a) M3.5, swept. **(b) M3.5, axisymmetric.**

(c) M3.0, swept. **(d) M3.0, axisymmetric.**

Fig. 26 In-plane turbulent shear stress field comparison between swept ($\ell = R_{TS}/4, \theta = 90°$) **and axisymmetric** ($\ell = 0$) **interaction behavior near impingement at** $\alpha = 13.5°$**.**

3. Separated Cases (α = 16°)

Figures 27 and 28 show the mean velocity behavior for axisymmetric interactions emanating from shock waves generated by α = 16° conical centerbody. Here, the significant increase in axial velocity defect is clear as well as the enlargement of the upstream influence of the interaction. Figure 29 shows the general rise in axial turbulence intensity, with the peak r.m.s. value of over $0.25\overline{u}_{1,\infty}$ at M3.5. Similarly, the turbulent shear stress is augmented significantly in the high-Mach cases with a much more pronounced region of positive shear near the wall.

For the axisymmetric configuration using this shock generator tip, a subset of the M3.5 data was processed using 16×16 final interrogation window size instead of 32×32 in order to assess the sensitivity to window size. Due to the increased computational effort required to process the new number of vectors (essentially 4×), processing the entire dataset at this increased resolution is not desired unless significant benefits are obtained. Directly comparing velocity data derived from the same set of images with the same vector acceptance criteria should elucidate the variation which stems directly from the interrogation window size. The resolved peak turbulence levels are expected to show the largest change. Hence, the case with highest turbulence was selected for this sensitivity study. Of course, smaller windows also mean less particles per interrogation region which decreases the fidelity of the correlation raising the level of noise in the measurement.

Figure 31 shows a comparison of the in-plane turbulent shear field which results from using smaller interrogation windows on the first two camera views for the M3.5 α = 16° axisymmetric case, which exhibited the highest level of turbulence in the interaction region. At this level of detail, the results appear nearly identical between the two window sizes with the primary difference being the smoothening of spatial variations with larger windows. To further examine the subtle differences driven by interrogation window size, Fig. 32 presents the difference in velocity values. The alteration in mean axial velocity result (Fig. 32a) is expectedly slight showing differences around 1% or less. For the turbulent stresses, very little deviation is observed, which implies that a more finely-resolved velocity field would not generate significantly higher peak turbulence levels. In fact, the primary affect appears to be an increase in freestream turbulence which is likely just an artifact of more noisy correlation peaks due to the reduced number of particles per window. Also, the reduction in valid vectors was $\approx$ 5 to 10% in the incoming boundary layer. All of this seems to support the idea that 32×32 windows were the correct choice for this dataset.

Figures 33 to 38 show comparisons of various flowfield quantities between the axisymmetric and swept cases for the high-Mach interactions in the near-interaction region at α = 16°. As with the other shock generator angles, the upstream influence is increased in the swept cases due to the 3D "relieving" effect of the shock sweep. Many of the same trends observed for α = 13.5° are reiterated here: the swept versions show (1) a reduced peak in $\overline{u'u'}$, (2) similar $\overline{w'w'}$ intensity, but spread further upstream of the impingement location, and (3) introduction of significant $\overline{u'w'}$, which exceeds the in-plane turbulent shear stress at M3.5.

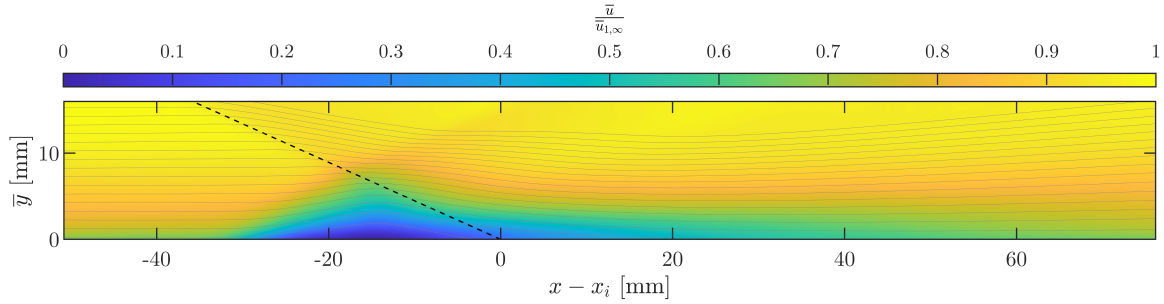

(a)

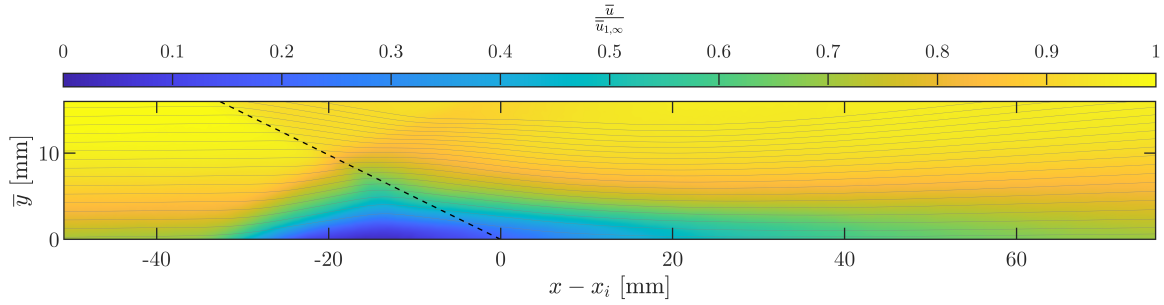

(b)

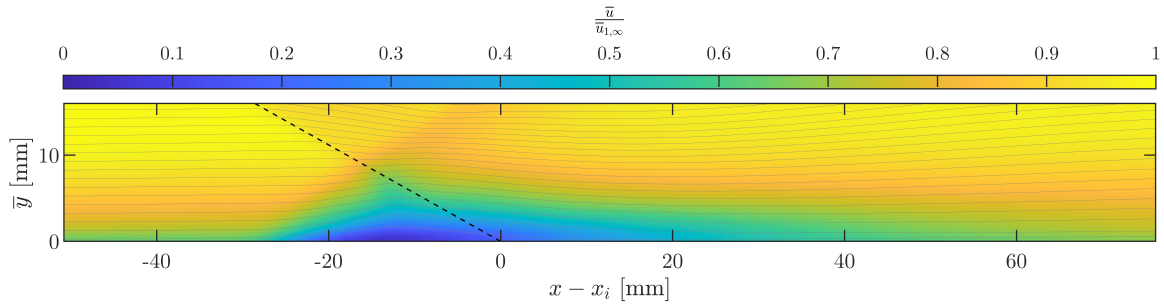

(c)

Fig. 27 Axial velocity fields in axisymmetric $\alpha = 16°$ interactions at (a) M3.5, (b) M3.0, and (c) M2.5.

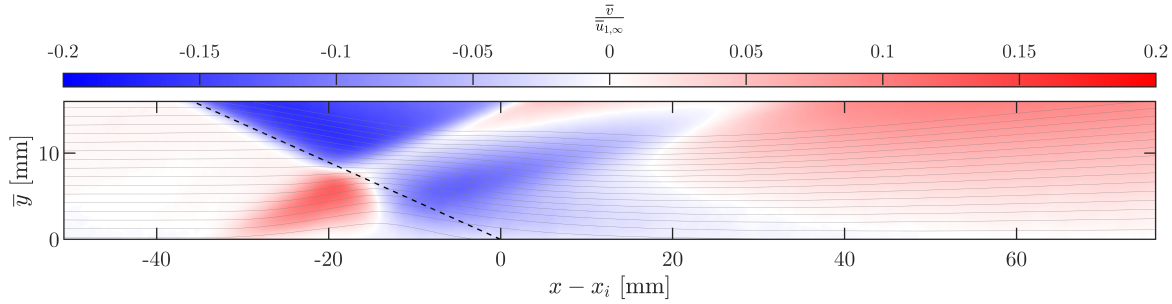

(a)

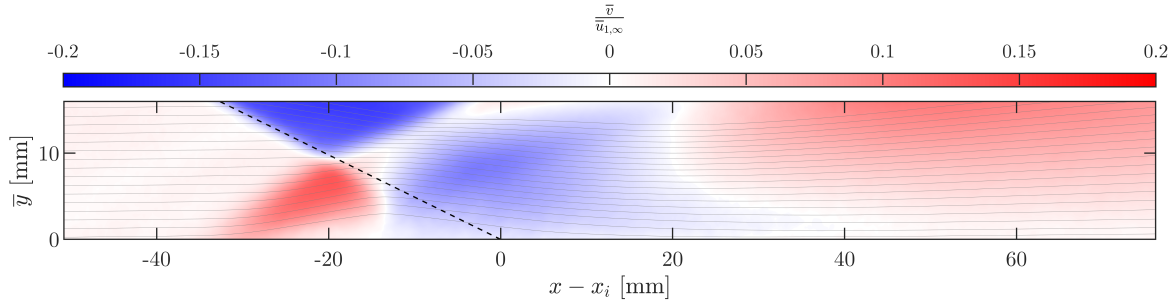

(b)

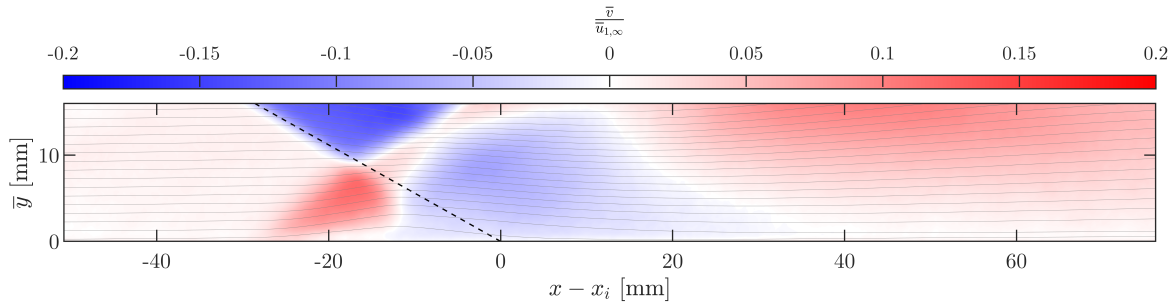

(c)

Fig. 28 Wall-normal velocity fields in axisymmetric $\alpha = 16°$ interactions at (a) M3.5, (b) M3.0, and (c) M2.5.

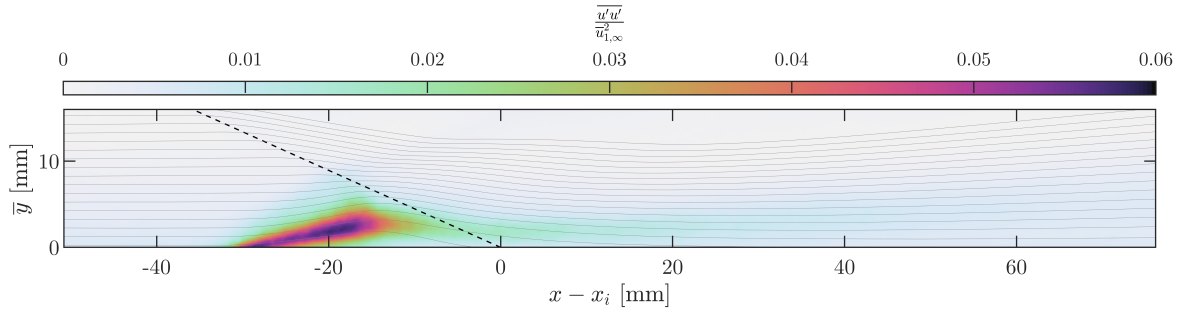

(a)

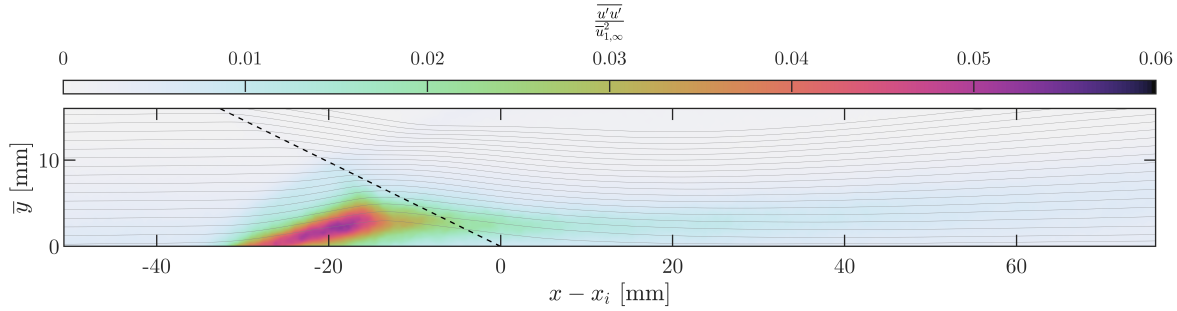

(b)

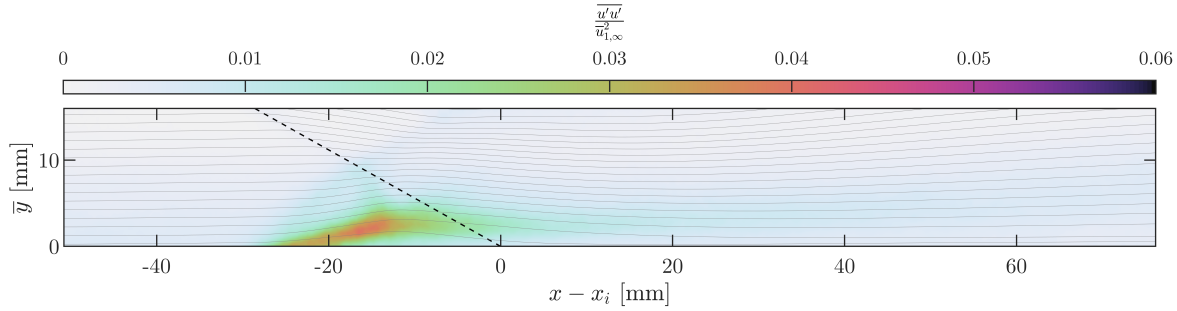

(c)

Fig. 29 Axial velocity turbulence intensity fields in axisymmetric $\alpha = 16°$ interactions at (a) M3.5, (b) M3.0, and (c) M2.5.

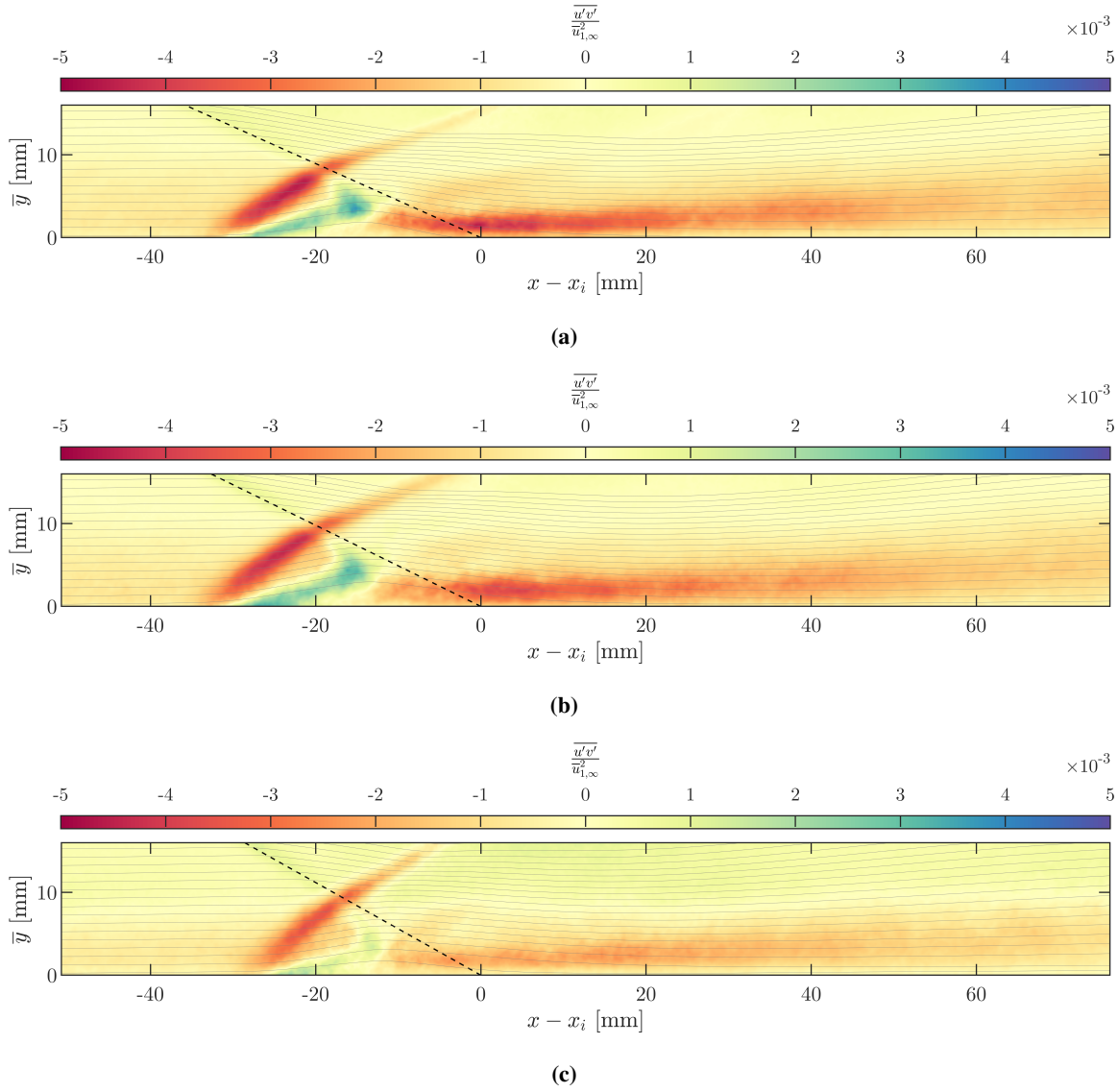

Fig. 30 Turbulent shear stress fields in axisymmetric $\alpha = 16°$ interactions at (a) M3.5, (b) M3.0, and (c) M2.5.

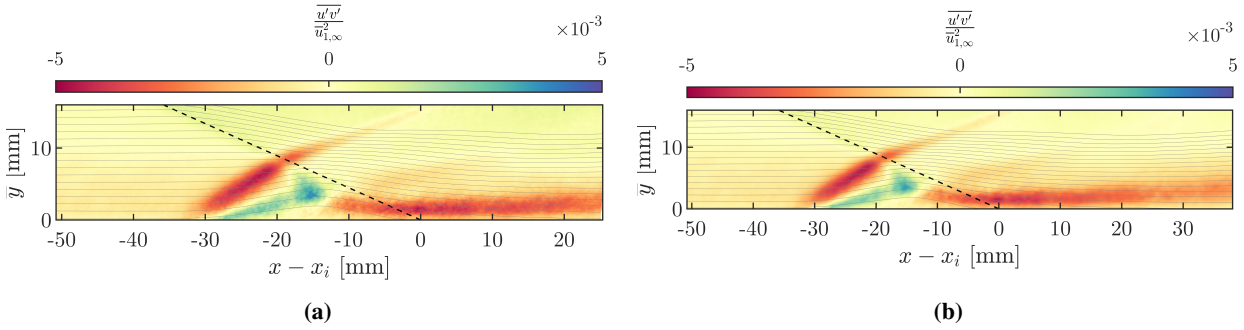

Fig. 31 Direct comparison of $\overline{u'v'}$ fields using (a) 16×16 final window size instead of (b) 32×32 for the axisymmetric $\alpha = 16°$ interaction at M3.5.

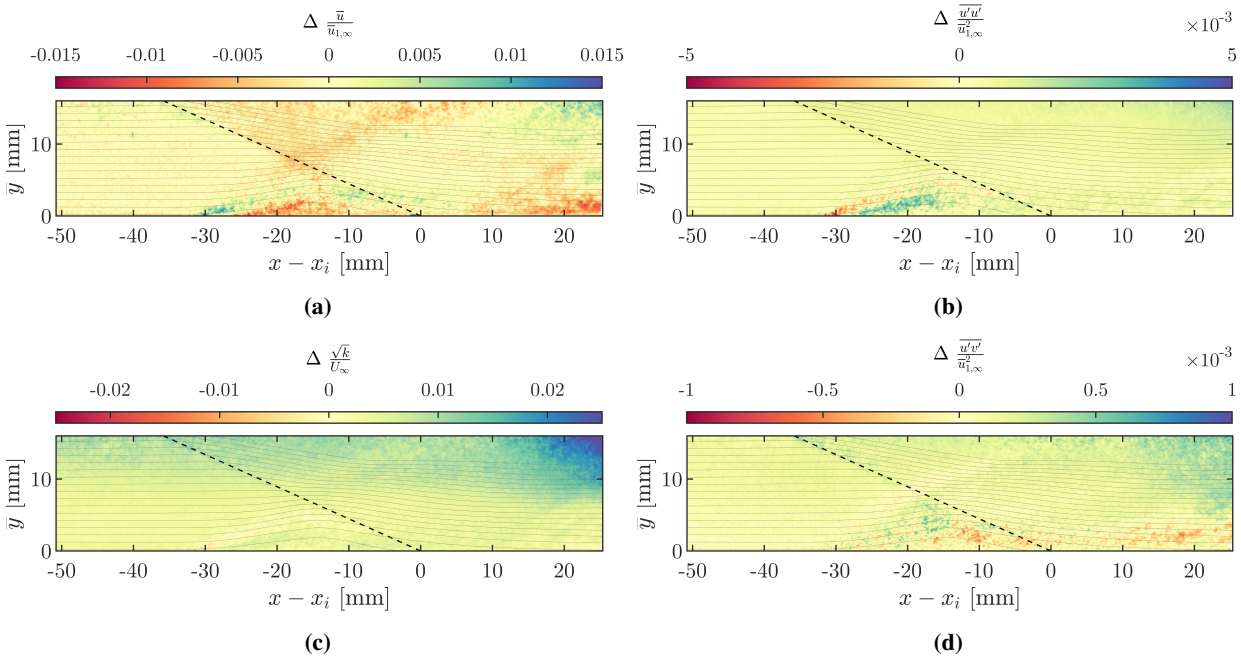

Fig. 32 Difference in mean velocity and turbulence intensities with 16×16 final window size instead of 32×32 baseline for the axisymmetric $\alpha = 16°$ interaction at M3.5.

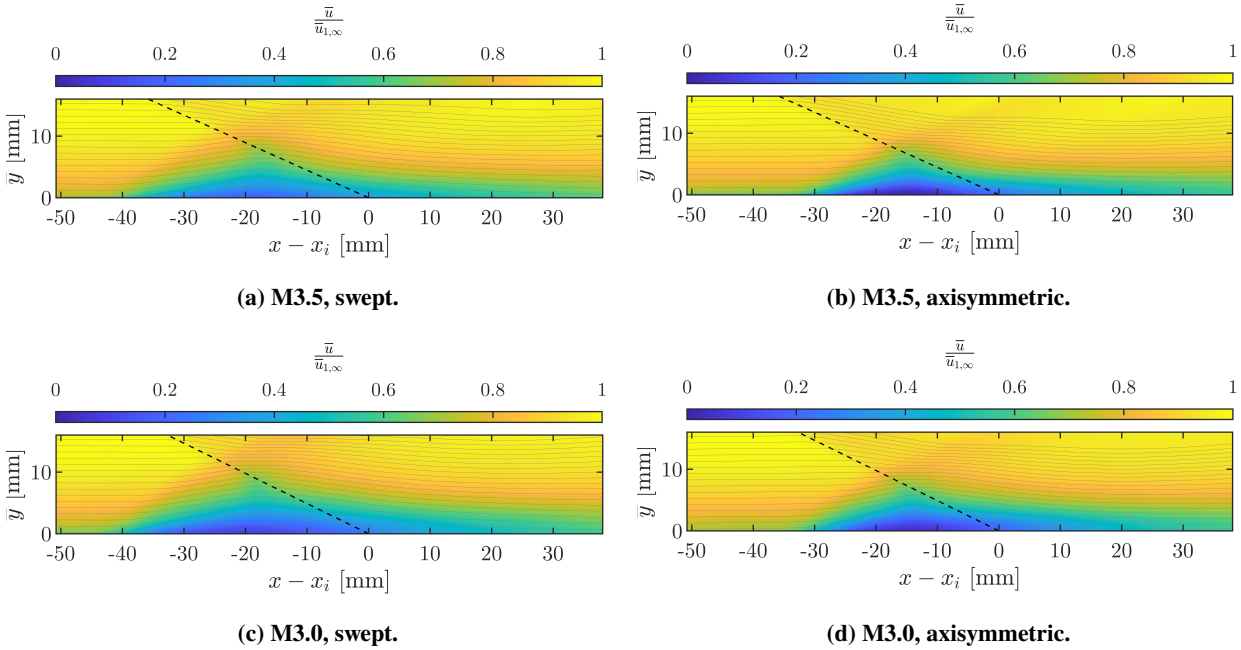

Fig. 33 Axial velocity field comparison between swept ($\ell = R_{TS}/4, \theta = 90°$) and axisymmetric ($\ell = 0$) interaction behavior near impingement at $\alpha = 16°$.

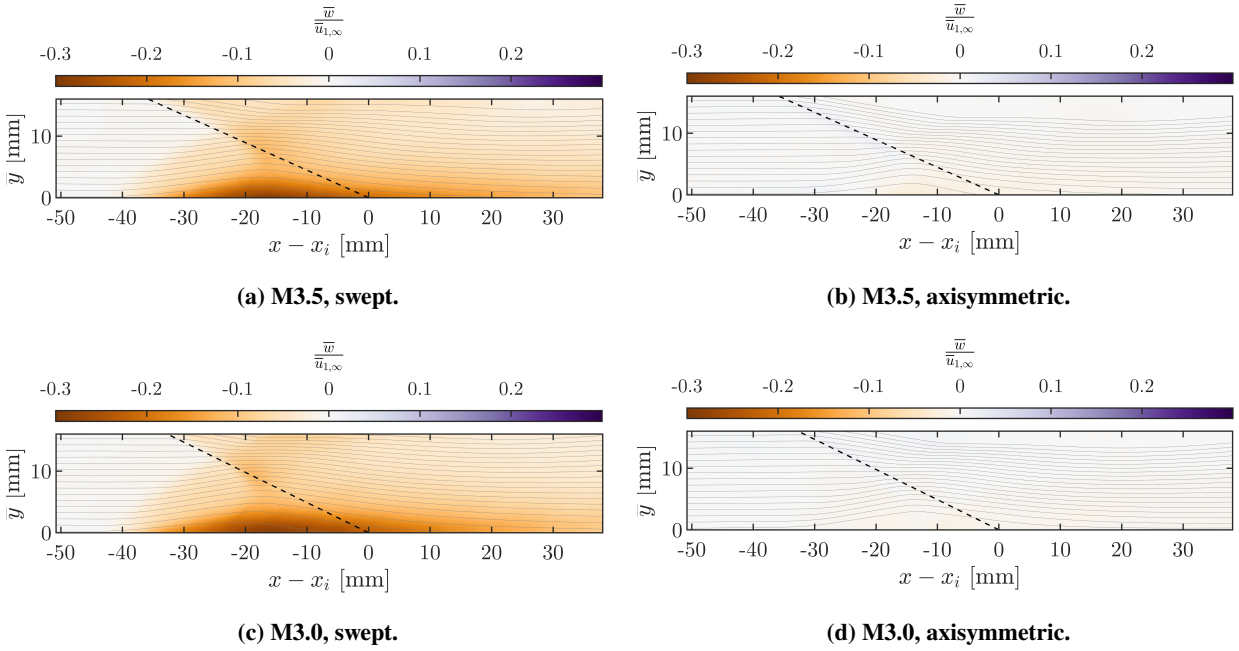

(a) M3.5, swept. **(b) M3.5, axisymmetric.**

(c) M3.0, swept. **(d) M3.0, axisymmetric.**

Fig. 34 Through-plane velocity field comparison between swept ($\ell = R_{TS}/4, \theta = 90°$) and axisymmetric ($\ell = 0$) interaction behavior near impingement at $\alpha = 16°$.

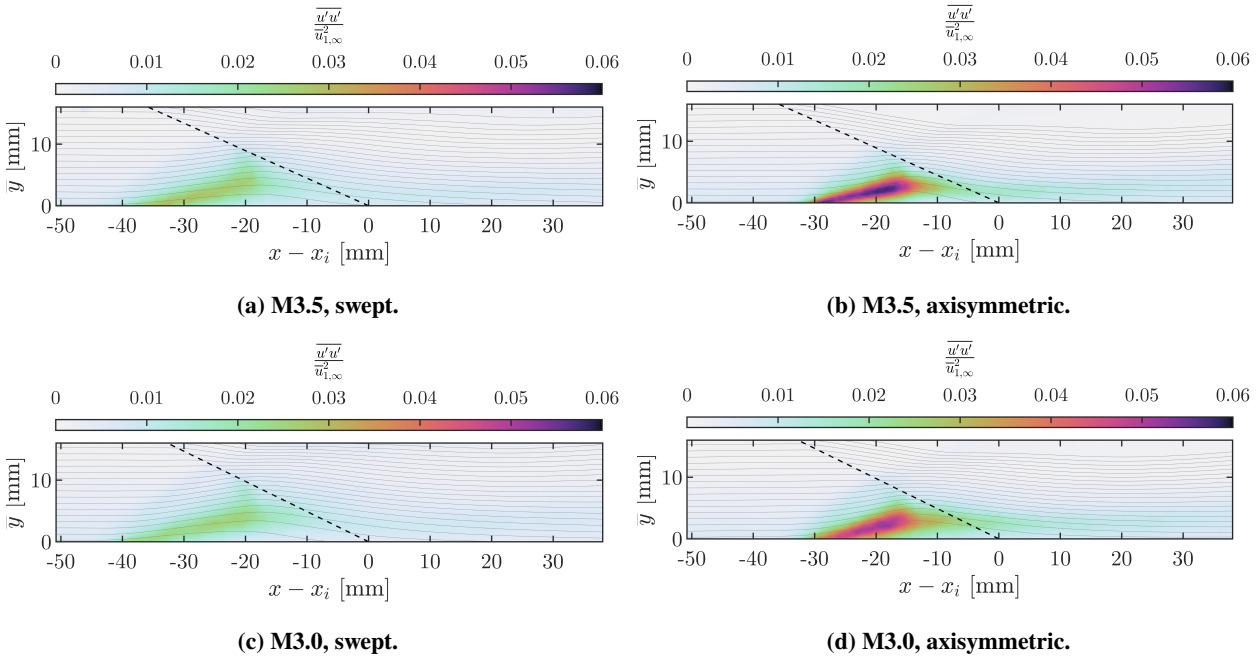

(a) M3.5, swept. **(b) M3.5, axisymmetric.**

(c) M3.0, swept. **(d) M3.0, axisymmetric.**

Fig. 35 Axial velocity turbulence intensity field comparison between swept ($\ell = R_{TS}/4, \theta = 90°$) and axisymmetric ($\ell = 0$) interaction behavior near impingement at $\alpha = 16°$.

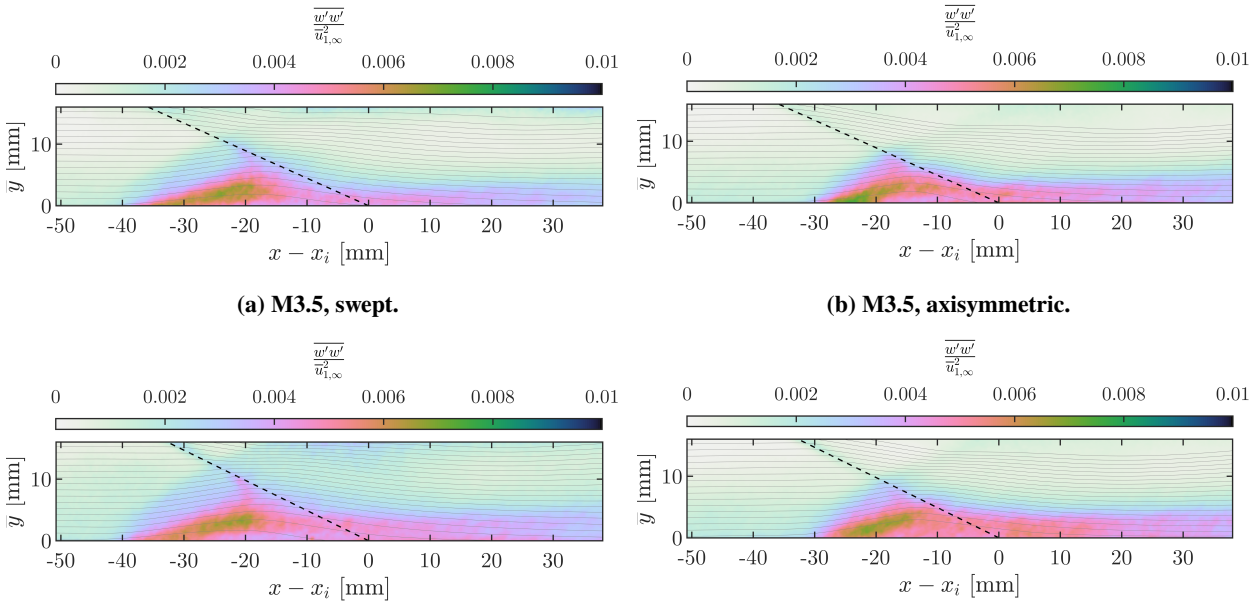

(a) M3.5, swept. **(b) M3.5, axisymmetric.**

(c) M3.0, swept. **(d) M3.0, axisymmetric.**

Fig. 36 Through-plane velocity turbulence intensity field comparison between swept ($\ell = R_{TS}/4, \theta = 90°$) and axisymmetric ($\ell = 0$) interaction behavior near impingement at $\alpha = 16°$.

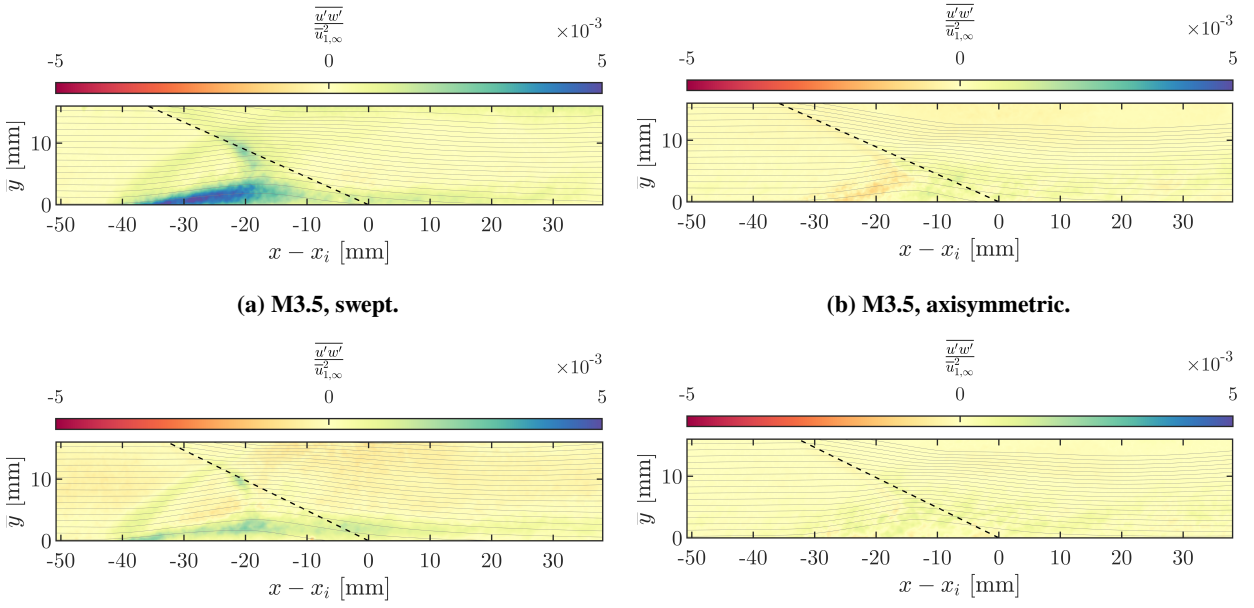

(a) M3.5, swept. **(b) M3.5, axisymmetric.**

(c) M3.0, swept. **(d) M3.0, axisymmetric.**

Fig. 37 x-z plane turbulent shear stress field comparison between swept ($\ell = R_{TS}/4, \theta = 90°$) and axisymmetric ($\ell = 0$) interaction behavior near impingement at $\alpha = 16°$.

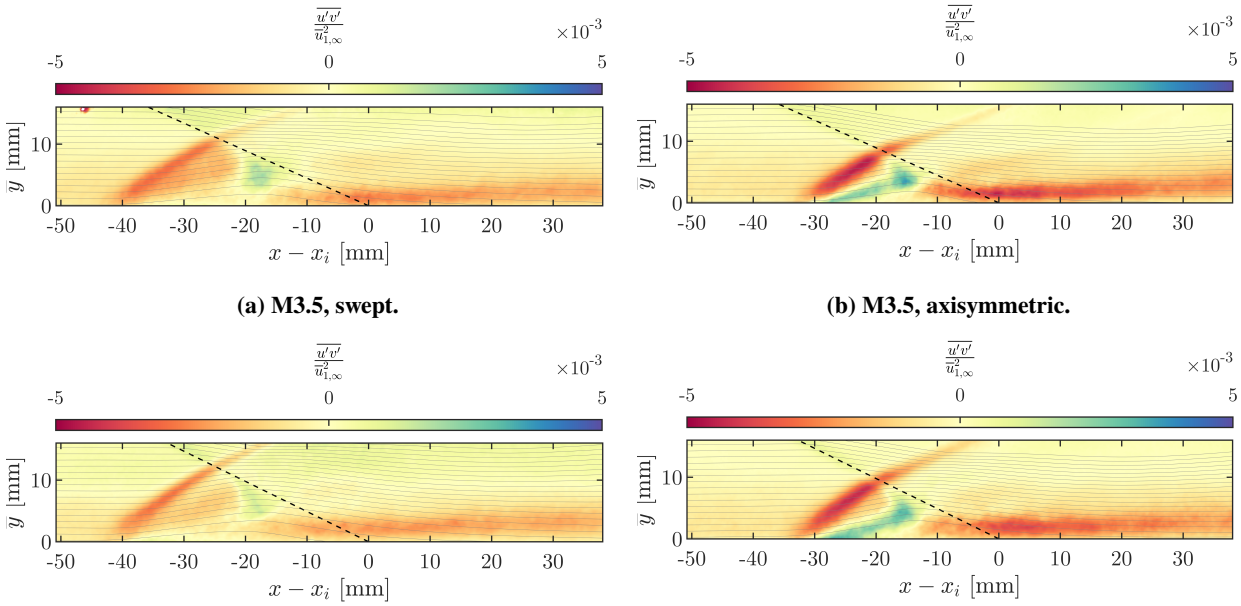

(a) M3.5, swept. **(b) M3.5, axisymmetric.**

(c) M3.0, swept. **(d) M3.0, axisymmetric.**

Fig. 38 In-plane turbulent shear stress field comparison between swept ($\ell = R_{TS}/4, \theta = 90°$) and axisymmetric ($\ell = 0$) interaction behavior near impingement at $\alpha = 16°$.

IV. Conclusions

This document summarizes the PIV data collection test entry completed in the summer of 2024 as part of the ongoing SWBLI experiments in the GRC 225 cm^2 Wind Tunnel at three nominal freestream Mach number conditions of 2.5, 3.0, and 3.5. Detailed post-processing methods utilized to quantify small offsets in the shock generator tip position are outlined and the results are collated herein. Thereafter, accounting for these small offsets, data are presented in coordinates which are referenced to consensus best-fit inviscid impingement locations to remove any sensitivity to displacements of the shock generator. Wall pressure profiles associated with the PIV test section are included as well for comparison with results from its "conventional" twin test section used for probe surveys.

PIV data are presented across the matrix of freestream Mach numbers and shock generator configurations in order to infer macroscopic trends in the data. In particular, the sensitivity of both the mean flow and turbulent behavior to variation in the freestream Mach number is illustrated. Overall, the quality of the data is exemplified by the detailed flow features which are resolved in the contour plots. Sensitivity of the velocity results to interrogation window size used for cross-correlation (spatial resolution) was investigated on a subset of the data and further reductions in window size below 32×32 pixels were found to have diminishing value.

Compiling the PIV data obtained in this test entry into a cohesive report provided an avenue to assess data quality in advance of the next test entry. There, select test points will be duplicated in order to assess repeatability of the results shown herein in addition to the exploration of test cases at reduced Reynolds number. The final overarching report will incorporate results from both entries along with comparisons to probe-based measurements across the HMVE campaign.

Support for this work was provided by NASA's Transformative Aeronautics Concepts Program through the Transformational Tools & Technologies (T^3) Project.

References

[1] DeBonis, J. R., Oberkampf, W. L., Wolf, R. T., Orkwis, P. D., Turner, M. G., Babinsky, H., and Benek, J. A., "Assessment of Computational Fluid Dynamics and Experimental Data for Shock Boundary-Layer Interactions," *AIAA Journal*, Vol. 50, No. 4, 2012, pp. 891–903. doi:10.2514/1.J051341.

[2] Settles, G. S., and Dodson, L. J., "Supersonic and hypersonic shock/boundary-layer interaction database," *AIAA Journal*, Vol. 32, No. 7, 1994, pp. 1377–1383. doi:10.2514/3.12205.

[3] Aeschliman, D. P., and Oberkampf, W. L., "Experimental Methodology for Computational Fluid Dynamics Code Validation," *AIAA Journal*, Vol. 36, No. 5, 1998, pp. 733–741. doi:10.2514/2.461.

[4] Babinsky, H., Oorebeek, J., and Cottingham, T., "Corner effects in reflecting oblique shock-wave/boundary-layer interactions," *51st AIAA Aerospace Sciences Meeting including the New Horizons Forum and Aerospace Exposition*, 2013, pp. 1–11. doi:10.2514/6.2013-859.

[5] Garnier, E., "Stimulated detached eddy simulation of three-dimensional shock/boundary layer interaction," *Shock Waves*, Vol. 19, No. 6, 2009, pp. 479–486. doi:10.1007/s00193-009-0233-7.

[6] Davis, D. O., "CFD Validation Experiment of a Mach 2.5 Axisymmetric Shock-Wave/Boundary-Layer Interaction," *Proceedings of the ASME/JSMA/KSME 2015 Joint Fluids Engineering Conference*, Fluids Engineering Division Summer Meeting, Vol. Volume 1: Symposia, 2015. doi:10.1115/AJKFluids20156342, v001T06A001.

[7] Sasson, J., "Conical Shock Wave Turbulent Boundary Layer Interactions in a Circular Test Section at Mach 2.5," Ph.D. thesis, Case Western Reserve University, 2022.

[8] Sasson, J., Reising, H. H., Davis, D. O., and Barnhart, P. J., "Summary of Shock Wave Turbulent Boundary Layer Interaction Experiments In a Circular Test Section," *AIAA SciTech 2023*, 2023. doi:10.2514/6.2023-0442.

[9] Reising, H. H., and Davis, D. O., "PIV Measurements of Shock-Wave/Boundary-Layer Interactions at Mach 2.5 in a Circular Test Section," *AIAA SCITECH 2024 Forum*, American Institute of Aeronautics and Astronautics, 2024. doi:10.2514/6.2024-2554.

[10] Reising, H. H., Sasson, J. S., Davis, D. O., Friedlander, D. F., and Howerton, L. W., "Cross-Measurement Comparisons for a CFD Validation Dataset on Mach 2.5 Axisymmetric Turbulent Shock-Wave/Boundary-Layer Interactions," *AIAA SciTech 2025*, 2025. doi:10.2514/6.2025-0474.

[11] Reising, H. H., and Davis, D. O., "Development and Assessment of a New Particle Image Velocimetry System in the NASA GRC 225 cm^2 Wind Tunnel," *AIAA SciTech 2023*, National Harbor, MD, 2023. doi:10.2514/6.2023-0631.